ORIGINAL PAPER

Evaluating the Microstructure Evolution Behaviors of Saturated Sandstone Using NMR Testing Under Uniaxial Short-Term and Creep Compression

Zhaofei Chu[1] · Zhijun Wu[1] · Quansheng Liu[1] · Lei Weng[1] · Zhiyang Wang[1] · Yuan Zhou[1]

Abstract

Understanding the micromechanical mechanism of the rock creep process is of great importance for studying the macroscopic time-dependent behavior of rocks. In this study, the evolution characteristics of the microstructure (cracks and pores) of saturated sandstones under short term and creep uniaxial compression conditions were investigated with the nuclear magnetic resonance (NMR) technique. The samples were first loaded to different stress levels and creep stages and then completely unloaded for NMR testing. Based on the testing results, the macroscopic deformation behavior, moisture migration law, pore size distribution, porosity, and microstructure change of the each sample under the short-term loading or different stages of creep were quantitatively analyzed. After that, by introducing a nonlinear elasto-viscoplastic damage creep model (EVP) by Zhao et al. (18:04017129, 2018), the relationships between the macroscopic irreversible strains and microscopic porosity increments were established. Overall, it was observed that: (1) regardless of the stress level, the magnitudes of the axial and lateral critical strains of samples at the onset of the accelerating creep stage are both relatively constant, and the axial strain is almost comparable to that at the peak stress in the short-term test, while the lateral strain is larger than that of the short-term test. (2) During the mechanical tests, the moisture in the samples migrates from large pores into small pores, and after mechanical tests, the porosities of the samples increase, in which the small pores always account for a larger proportion. (3) Corresponding to the three creep stages, the porosity of the sample increases slightly after the transient stage, increases to a constant value that is largely independent of stress after the steady stage, and increases significantly after the creep failure. In particular, compared to the initial porosity of 6.7%, the average porosities of samples taken to the onset of the tertiary stage and creep failure is 7.49% and 8.71%, increasing by 16.7% and 29.8%, respectively. (4) The porosity growth of sandstone during the brittle creep is mainly driven by the microscopic subcritical crack growth along the grain boundaries.

Keywords Saturated sandstone · Microstructure · Porosity · Nuclear magnetic resonance (NMR) · Creep test

Abbreviations

NMR	Nuclear magnetic resonance
XRD	X-ray diffraction
SEM	Scanning electron microscope
UCS	Uniaxial compressive strength
EVP creep model	Nonlinear elasto-viscoplastic creep constitutive model

List of symbols

σ_0	Axial creep stress
T_2	Transverse relaxation time
T_{2S}	Transverse surface relaxation time
ρ_2	Surface relaxivity
r	Radius of pores
σ_P	Stress at the inflection point of rock compaction and dilatancy
$\varepsilon_a, \varepsilon_l, \varepsilon_v$	Axial, lateral, and volumetric strains of the sample
t_{S2}, t_f	Time-to-onset of accelerating stage and time-to-failure
T_2 cutoff	Relaxation time separating mobile from immobile water
ϕ	Porosity
ϕ_{Si}	Initial porosity
ϕ_{S0}	Porosity after short-term loading
ϕ_{S1}	Porosity after transient creep stage

✉ Zhijun Wu
wuzh0013@e.ntu.edu.sg

1 School of Civil Engineering, Wuhan University, No. 8 Donghu South Road, Wuhan 430072, China

ϕ_{S2}	Porosity after transient and steady creep stage
ϕ_{S3}	Porosity after creep failure
ϕ_s, ϕ_l	Porosity contributed by small pores and large pores
D	Creep damage variable
σ_s	Long-term strength
E_{ie}, E_{ip}	Instantaneous elastic modulus and plastic modulus
E_{ve}, η_{ve}	Viscoelastic parameters
E_{vp}, η_{vp1}	Viscoplastic parameters
η_0	Initial viscosity coefficient
η_{vp2}	Viscoplastic viscosity coefficient
k, γ	Material constants in EVP creep model
$\varepsilon_{ie}, \varepsilon_{ip}$	Instantaneous elastic and plastic strains
ε_{vp}	Viscoplastic strain
D_{S2}	Creep damage variable at the onset of accelerating stage

1 Introduction

The time-dependent behavior of rock, i.e., creep, is a fundamental and pervasive phenomenon in geotechnical engineering, such as deep tunnels, mining, and slopes, and thus usually has a critical effect on the long-term safety of supporting structures (Chu et al. 2021; Guayacán-Carrillo et al. 2018; Liu et al. 2020; Wu et al. 2020). Sandstone, commonly encountered in engineering, generally has a large proportion of pores and strong creep behavior, especially in a saturated state (Ma et al. 2019; Ngwenya et al. 2001; Tang et al. 2018; Yu et al. 2020). Extensive laboratory creep tests on different types of saturated sandstones have shown that creep deformation can account for 20–50% of the total deformation (Tsai et al. 2008; Yang and Jiang 2010; Zhang et al. 2015), and in extreme cases can even exceed 80% (Tian et al. 2015; Zheng et al. 2015). Similar to most soft rocks, the creep behavior of sandstone usually exhibits a typical three-stage characteristic over time, namely, primary or transient creep, secondary or steady-state creep, and tertiary or accelerating creep (Yang et al. 2014a, b; Yu et al. 2019). However, unlike compact rocks, such as mudstone or argillaceous slate, the creep behaviors of sandstone, due to its porous nature, are caused not only by intergranular cracking but also by the collapse of large intergranular pores (Wong and Baud 2012; Wu et al. 2000). Therefore, for the brittle creep analysis of sandstone, the major challenge is to understand how and to what extent microscopic (grain-scale) time-dependent pore (or crack) growth processes are linked to the observed macroscopic mechanical behaviors (Brantut et al. 2014a, b; Brantut et al. 2013).

Mechanistically, whether a creep process or a general loading process occurs, the macroscopic deformation and failure of rocks mainly result from the coalescence of many microscopic, grain-scale cracks and collapse of voids (Abdallah et al. 2021; Cong et al. 2020; Fan et al. 2020; Paterson and Wong 2005). Previous theoretical studies on rock brittle creep have demonstrated that the time-dependent behavior of rock under constant stress conditions can be essentially attributed to chemically activated subcritical crack growth processes, which are referred to as stress corrosion reactions (Amitrano and Helmstetter 2006; Brantut et al. 2014a, b). To explain this physical mechanism, several micromechanical approaches have been proposed to establish the link between subcritical crack growth and the macroscopic time-dependent behavior of rocks (Brantut et al. 2012; Costin 1983; Li et al. 2020; Main 2000). For example, based on fracture mechanics, N. Brantut et al. (2012) proposed a micromechanical model that combines the sliding wing cracking laws of Ashby and Sammis (1990) and the subcritical crack propagation laws of Charles (1958) to describe the macroscopic brittle creep behavior of rocks. Nevertheless, the real propagation process and spatial distribution of microscopic cracks and pores induced by stress corrosion still need to be quantitatively analyzed via laboratory tests, which is also a prerequisite for micromechanical analysis (Fan et al. 2018; Li and Shao 2016).

In terms of creep tests on sandstone, most of previous studies have placed emphases on analyzing the macroscopic mechanical behavior of samples under different environmental and stress conditions, such as high temperature, fluid pressure, and chemical corrosion (Ma et al. 2019; Noël et al. 2019; Tang et al. 2018; Yang et al. 2018; Yang and Hu 2018; Yu et al. 2019; Zheng et al. 2015; Zhu et al. 2019). Correspondingly, the creep deformation, permeability, failure mode, and other macroscopic characteristics of different sandstone samples have been systematically investigated as well (Brantut et al. 2014a, b; Wong and Baud 2012). However, for microstructural analysis of sandstone during creep, by contrast, only a few studies based on acoustic emission (AE) monitoring, optical microscopy, and SEM have been reported previously (Baud and Meredith 1997; Heap et al. 2009; Ngwenya et al. 2001; Yang et al. 2014a, b). For example, through microscopic optical analysis on four types of sandstones after creep failure, Ngwenya et al. (2001) found that macroscopic brittle creep behavior was characterized by dilatant microcracking, which resulted in shear localization along narrower fracture zones. Using AE monitoring and optical microscopy simultaneously, Heap et al. (2009, 2015) investigated the spatial development of sample damage during brittle and ductile creep and the microcrack density following creep deformation. Their results shown that the aggregation and localization of damage increased as creep progresses, with the greatest changes occurring in the

tertiary stage. Moreover, compared to the initial undeformed state, approximately 24–37% increases in crack density at the onset of tertiary stage during brittle creep. Similarly, using SEM, Yang et al. (2014a, b) investigated the crack distributions of red sandstone subjected to creep tests with different fluid pressures, and found that with increasing pore pressure, the arrangement of mineral grains becomes denser and the microcracks decrease in number. In addition, combining the stress–strain curve and wave velocity characteristics under uniaxial compression, Cao et al. (2014) analyzed the microstructure change of sandstone creep and determined the critical stresses for secondary and tertiary creep. However, the growth of microcracks and the evolution of pores at different creep stages and creep stresses were not quantitatively analyzed.

Regarding laboratory tests, both optical microscopy and SEM are 2D observation methods, which cannot quantitatively analyze the microstructure evolution of a whole sample due to their observation range limitations (Fan et al. 2018; Wu et al. 2000). For AE monitoring, although it is a three dimensional testing method that can monitor the entire creep process in real time, it can only locate damage inside the sample through the signals originated from large cracks, but not quantify the size and distribution of microscopic cracks or pores (Weng et al. 2019). In contrast, the low-field NMR technique, a recently developed method, can measure the microscopic pore and crack features of rocks with obvious considerable advantages in effectiveness, accuracy (approximately 0.1 nm), and speed (Cai et al. 2014; Shen et al. 2020). In particular, through inversion of water-containing signals of pores or cracks at different scales, the pore size distribution and porosity of samples can also be obtained by the NMR technique (Lin et al. 2020). Based on this technique, many microscopic studies associated with short-term mechanical tests of sandstone under different conditions have been conducted, which mainly involve static loading, dynamic impact, freezing and thawing, and chemical corrosion (Gao et al. 2017; Hao et al. 2020; Lyu et al. 2020; Shen et al. 2020; Wang et al. 2020a, b; Weng et al. 2018, 2021; Xue et al., 2018). However, the application of NMR technique to the creep experiments of rock is relatively rare, especially for detecting the damage changes during the creep stage. To date, only Cheng et al. (2021a, b) have undertaken a preliminary investigation on the microcracking characteristics of sandstones after creep using this technique. However, in their work, the pore characteristics of samples after experiencing different stages of creep at different stress levels were not investigated and the moisture migration laws within samples during instantaneous loading and creep loading were also not concerned.

Accordingly, in this paper, the microstructure (cracks and pores) characteristics of saturated sandstone samples under short-term loading and long-term creep processes are

systematically investigated by the NMR testing method. In the mechanical tests, the sandstone samples first were loaded to eight different levels of stress, then underwent different stages of creep under each constant stress, and finally were completely unloaded. In the NMR tests, the sandstone samples were measured three times before loading, immediately after unloading, and after being resaturated. Macroscopic creep deformation behaviors (including the creep strain, steady-state creep rate, and critical creep time) under different conditions were systematically studied. The changes in the NMR T_2 spectrum distribution and porosity of the samples after being subjected to different creep stresses and creep stages were quantified and analyzed. On this basis, the moisture migration law, microscopic crack and pore evolution, and microdamage mechanisms of the sample during short-term loading and creep were investigated in combination with SEM observations. Finally, by introducing a nonlinear elasto-viscoplastic damage creep model proposed by Zhao et al. (2018), the elasto-viscoplastic strains of the sample under each stress level were separated, and creep damage was conducted by considering the porosity.

2 Experimental Methodology

2.1 Sample Preparation

The rock used in this study is red sandstone from a hydropower station slope in Yunnan Province, and was cored from a single block without macroscopic cracks to ensure the reliability of the test results. Figure 1a shows the microscopic photographs of the red sandstone sample, Fig. 1b shows the grain size distribution, and Fig. 1c and d show its SEM microphotographs. Clearly, this red sandstone is a granular cementitious material with medium-sized grains of approximately 0.01–0.3 mm. Moreover, according to X-ray diffraction (XRD), its mineral contents are listed in Table 1.

In the study, the dimensions of the samples were 50 mm in diameter and 100 mm in height. To reduce the differences between the samples, all the sandstone samples were cored from the same rock mass. Moreover, to further ensure the uniformity of the samples, the density, P-wave velocity and initial porosity of the prepared sandstone samples were first measured prior to performing the mechanical tests. Figure 2a shows the lateral and vertical P-wave velocities of the 40 samples employed in this research, which were measured with the ultrasonic pulse apparatus. The average P-wave velocity of all samples is approximately 2400 m/s. Figure 2b shows the corresponding T_2 spectra of those samples tested by the NMR technique. In fact, the NMR T_2 spectrum is the water content distribution of different sizes of pores and the area of the curve is the porosity of the sample. Therefore, the average
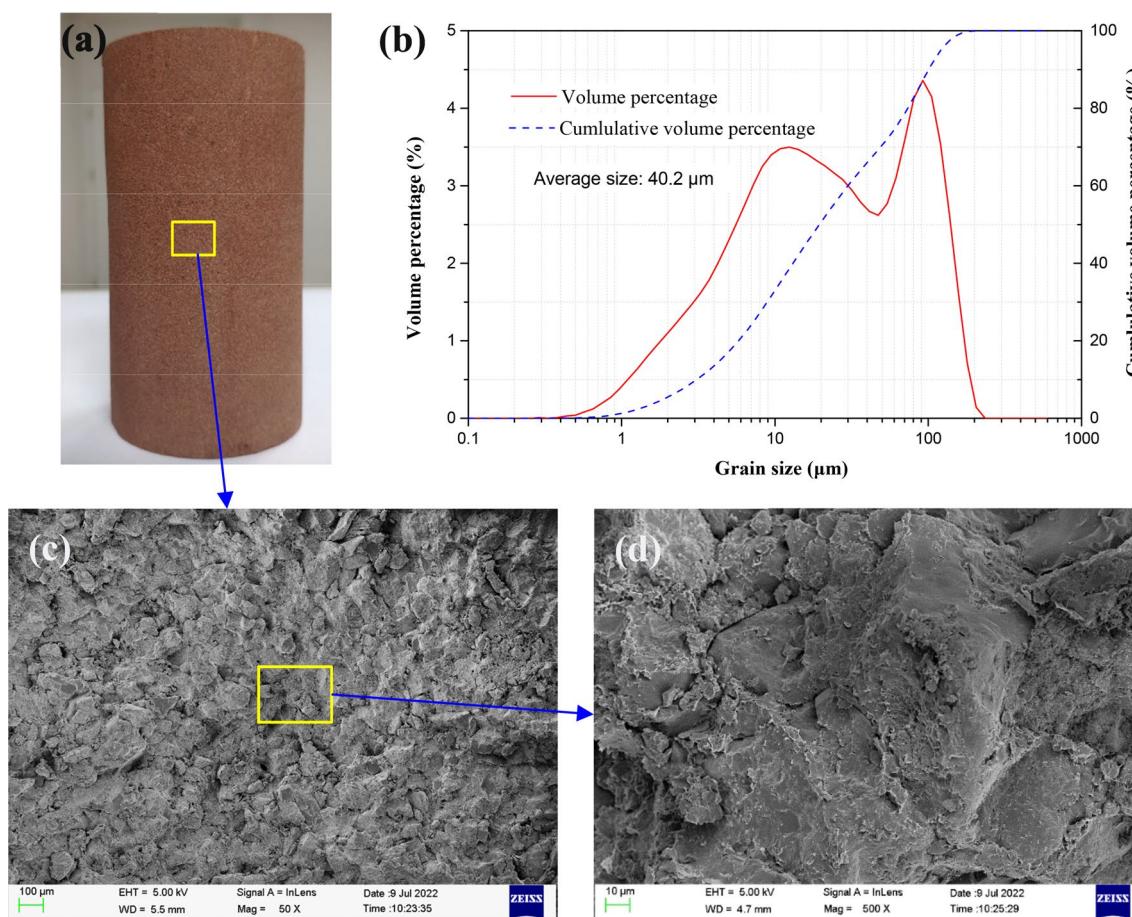
Fig. 1 a Photographs of Yunnan red sandstone specimen, **b** grain size distribution, **c** and **d** microphotographs taken by SEM, under ×50 and ×500 magnifications, respectively

Table 1 Mineral contents and petrophysical parameters of the red sandstone

Mineral contents based on XRD		Petrophysical parameters	
Quartz, %	48.12	P-wave velocity, m/s	2400
Feldspar, %	30.51	Initial porosity, %	6.7
Calcite, %	7.92	UCS, MPa	48.32
Hematite, %	3.07	Poisson's ratio	0.35
Clay, %	6.64	Elastic modulus, MPa	8.75
Others, %	3.74	–	–

initial porosity of this red sandstone is 6.7%. In addition, to further understand the petrophysical properties of this red sandstone, uniaxial compressive strength (UCS) tests were performed on three saturated samples. The average UCS, elastic modulus E and Poisson's ratio ν are summarized in Table 1.

2.2 Experimental Scheme and Procedure

In this paper, two types of tests were carried out: mechanical tests and NMR tests. The mechanical tests include the short-term uniaxial compression test and creep compression test. The short-term loading test refers to the monotonic uniaxial compression test with the loading rate of 0.2 MPa/s (see Fig. 3a). The end point of each short-term loading level is equal to the preset creep stress, and once the stress has reached the target value, it is immediately unloaded to zero for NMR tests. Table 2 shows the detailed testing scheme of the mechanical test, where as expected, the factors of the stress level and creep stage are taken into account. Specifically, to account for the influence of the stress level, the uniaxial compression stress σ_0 was divided into eight levels (i.e., $\sigma_0 = 0.48$–0.95UCS). Similarly, to consider the influence of different creep stages, for each stress level, the samples underwent creep to the end of the transient stage (S1), onset of the accelerating stage (S2), and final failure (S3), where the positions of S1, S2 and S3 are shown in Fig. 3b. However, when $\sigma_0 = 0.48$UCS and 0.58UCS, the samples
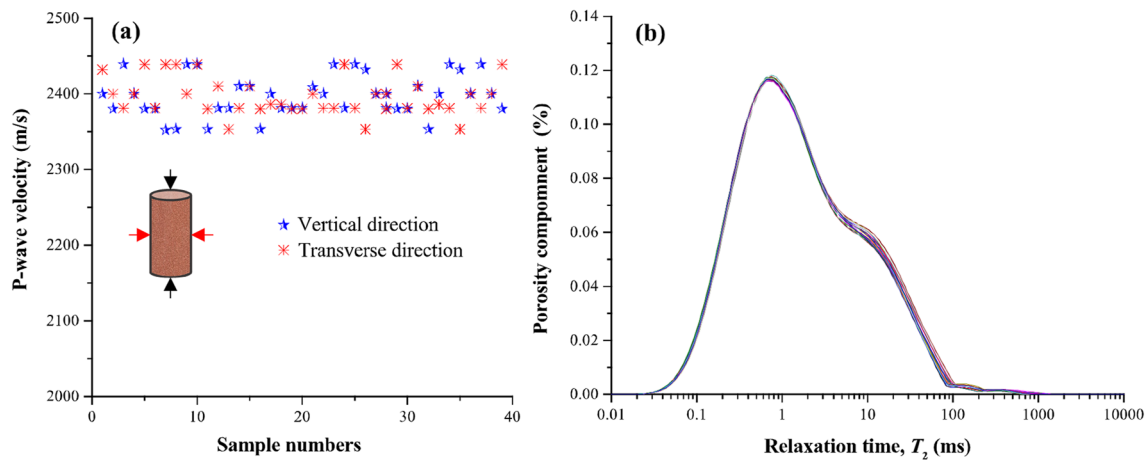
Fig. 2 **a** Initial P-wave velocity and **b** T_2 distribution of the chosen samples
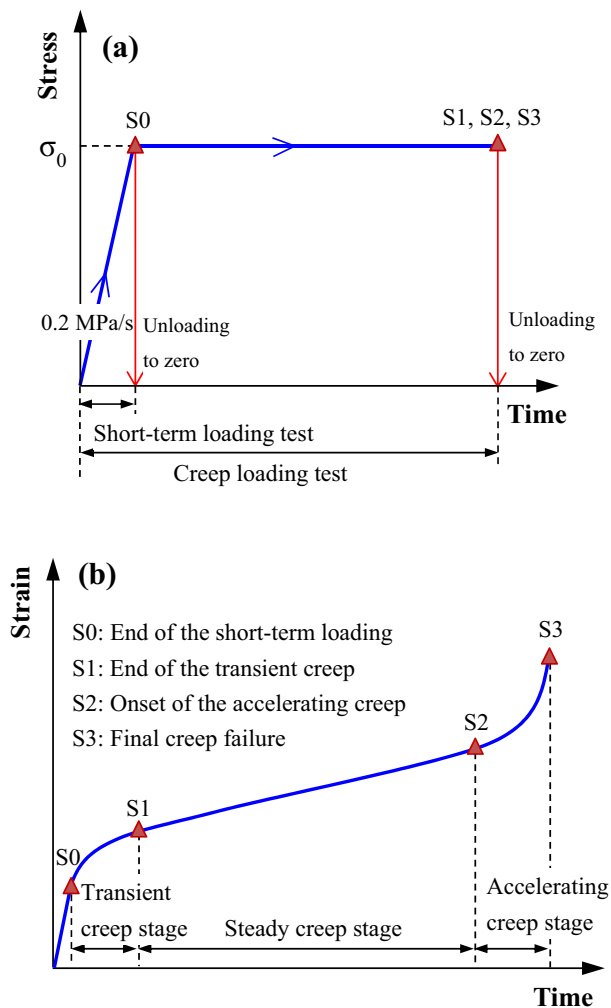

Fig. 3 Illustrations of **a** two kinds of loading tests and **b** different creep stages and the meanings of the states of S0–S3

could not reach the accelerating stage due to the lower stress, and even at the steady stage, the creep rates are very small. Therefore, only the transient creep stage was considered for these two stress levels. In addition, when $\sigma_0 = 0.95UCS$, the transient creep stage of the samples could not be precisely captured since the total creep durations are quite short. As a consequence, the tests of only the steady and accelerating creep stages are listed in Table 2 for this stress level.

For the mechanical testing process, short-term tests were first conducted on samples P1 to P8. After that, since the creep behavior of the sandstone under different stress levels is unknown prior to the tests, the inflection points associated with the three creep stages (i.e., S1, S2 and S3 in Fig. 3b) cannot be easily and accurately determined from the creep curves. Therefore, during the creep testing, we first carried out creep tests on the samples C1-1, C2-1, C3-3, C4-3, C5-3, C6-3, C7-3 and C8-3 to characterize the entire creep process and behavior of the sandstone under each stress level. Based on the testing results, the strains, strain rates, and creep time at the inflection points of S1 and S2 were preliminarily estimated, providing a reference target value for subsequent creep tests. Then, creep tests were sequentially carried out on samples C3-2 to C8-2 and C3-1 to C7-1, corresponding to creep stages to S2 and S1, respectively. However, due to the sample variability, both the axial strain and strain rate of the above samples during creep were monitored in real time, and once the estimated values at S1 and S2 were reached, the samples were slowly unloaded.

The detailed research procedures consists of the following steps: (1) Sample grouping and initial NMR testing. According to the test scheme listed in Table 2, the sandstone samples should be divided into 8 groups before testing, with 5 samples in each group, for a total of 40 samples. For each group, four samples were designated for testing, and one was reserved as a backup. Before the mechanical testing, all the

Table 2 Testing scheme of the mechanical tests

| Load level σ_0 | Short-term test | Creep test | | |
	Load to S0	Creep to S1	Creep to S2	Creep to S3
0.48UCS, 22.93 MPa	P1	C1-1	–	–
0.58UCS, 28.03 MPa	P2	C2-1	–	–
0.69UCS, 33.12 MPa	P3	C3-1	C3-2	C3-3
0.74UCS, 35.67 MPa	P4	C4-1	C4-2	C4-3
0.79UCS, 38.22 MPa	P5	C5-1	C5-2	C5-3
0.84UCS, 40.76 MPa	P6	C6-1	C6-2	C6-3
0.90UCS, 43.31 MPa	P7	C7-1	C7-2	C7-3
0.95UCS, 45.86 MPa	P8	-	C8-2	C8-3

UCS is the uniaxial compressive strength, and S0–S3 are shown in Fig. 3
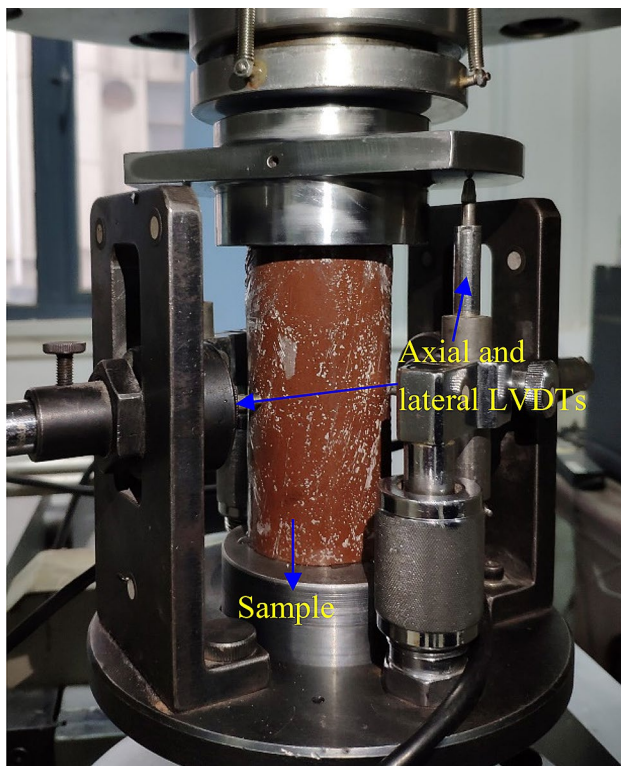
Fig. 4 Mechanical test photo of the sample

samples were saturated by a vacuum saturator for 48 h and tested by the NMR system to obtain the initial porosity, T_2 spectra and pore volume. (2) Mechanical testing. Short-term tests and creep tests were performed to obtain the short-term and creep behaviors of sandstones subjected to different levels of stress. Notably, the samples for each stress level and creep stage were independent. To prevent the evaporation of water inside the sample, the surface of the sample during mechanical tests was always tightly sealed by the water-proof membrane, and its axial and lateral deformations were recorded simultaneously, as seen in Fig. 4. (3) NMR testing: After the samples were unloaded, NMR tests were carried

out immediately to investigate the moisture migration in samples during the loading and creep process. Afterwards, the samples were resaturated for 48 h in vacuum saturator and retested by the NMR system. The porosity, T_2 spectrum and pore volume under varying stress levels and creep stages were studied and compared with those of the initial state.

2.3 Experimental Setup

In this study, the short-term uniaxial compression test and creep uniaxial compression test were conducted on an MTS 815 testing machine, which is capable of applying a stable servo-controlled axial load. The maximum axial load capacity of the testing machine was 2600 kN. The axial and lateral deformation of the samples were measured with linear voltage differential transducers (LVDTs) with an accuracy of 10^{-3} mm. During creep tests, the initial loading rate was the same as that of the instantaneous test, which was set to 0.2 MPa/s. After the target stress was reached, the stress was held constant using a servo-control system with a control accuracy of ± 0.2 kN. In addition, the room temperature was maintained at 25 °C.

NMR tests were performed using a MacroMR12-150H-I system (produced by Suzhou Niumag Analytical Instrument Corporation, Suzhou, China) with a constant magnetic field strength of 0.28 T and a resonance frequency of 12.534 MHz (Weng et al. 2021). The main components of the system were a controller, a spectrometer subsystem, a RF unit and a gradient unit. The basic principle of NMR technology has been introduced in detail in previous literatures (Li et al. 2018; Xue et al. 2018). Notably, the transverse relaxation time, T_2, is generally determined by three different relaxation types (bulk relaxation, surface relaxation, and diffusion relaxation) for a porous material. However, for water-saturated rocks, the bulk and diffusion relaxations can be disregarded (Chen et al. 2018; Liu et al. 2018). Therefore, the measured NMR T_2 value is mainly related to surface relaxation, which can be simply expressed as follows (Li et al. 2018; Weng et al. 2018; Zhou et al. 2018a, b):

$$\frac{1}{T_2} \approx \frac{1}{T_{2S}} = \rho\left(\frac{S}{V}\right)_{\text{Pore}}, \tag{1}$$

where T_2 is the transverse relaxation time (ms); T_{2S} is the transverse surface relaxation time (ms); ρ_2 is the surface relaxivity (µm/s), which generally equals 0.05 µm/ms for sandstones; and S/V is the surface-to-volume ratio of the pore (m^{-1}), which is equal to $2/r$ (r is the radius of pores) here because the pores in the rock material are assumed to be cylindrical (Li et al. 2018). Therefore, substituting all the given quantities into Eq. (1), the relation between the pore radius and the relaxation time T_2 of the sandstone is rewritten as: $r = 0.1T_2$ (µm). Clearly, T_2 is proportional to the pore size; the smaller T_2, the smaller the pore size.

3 Experimental Results

3.1 Creep Mechanical Behavior

Figure 5 shows the stress–strain relationships of the sandstone under different creep stress levels, which were obtained from samples C1-1, C2-1, C3-3, C4-3, C5-3, C6-3, C7-3 and C8-3. As shown in Fig. 5a, the axial and lateral loading curves under the eight stress levels show good consistency, indicating that the selected samples have good uniformity and that the problem of sample variability is eliminated. Figure 5b shows the volume stress–strain curves, along which points C and D are the microcrack initiation point and the volumetric strain inflection point, respectively. In general, the stresses (σ_C and σ_D) at these two points are the thresholds for stable and unstable crack growth. For this saturated sandstone, σ_C and σ_D are approximately equal to 20.8 MPa and 34 MPa, corresponding to 43%UCS and 70%UCS, respectively. The σ_C was calculated with crack volumetric strain (CVS) method (Nicksiar and Martin 2013). With regard to rock creep, σ_C is generally considered to be a threshold for judging creep stability or failure, above which the samples will finally collapse due to plastic or viscoplastic deformation (Brantut et al. 2014a, b; Heap et al. 2009). For this reason, in some studies (Chandler 2013; Deng et al. 2016; Zhou et al. 2018a, b), σ_C is also regarded as the long-term strength. However, if the applied creep stress is equal to or slightly greater than this value, the creep failure time of sample is likely to be very long. Therefore, in this paper most of the creep stresses are larger than this value to ensure the distinct three-stage creep behavior of the samples within an acceptable time scale in laboratory.

As shown in Fig. 6, when the creep stress is greater than or equal to 33.12 MPa (i.e., 69%UCS), the creep failure of samples can be observed, with the maximum and minimum creep time of 9,200 and 72 min. Moreover, the figure shows that when $\sigma_0 = 22.93$ MPa and 28.03 MPa, basically only the

transient creep stage is observed, while for $\sigma_0 \geq 33.12$ MPa, the samples exhibit a typical three-stage creep characteristic. Therefore, corresponding to the following NMR porosity test, the creep tests at $\sigma_0 \geq 35.12$ MPa were performed on samples C3-2 to C8-2 and C3-1 to C8-1, where samples C3-1 to C8-1 only creep to the end of the transient creep stage, while samples C3-1 to C8-1 creep to the onset of the accelerating creep stage.

Figure 7 shows the creep curves of all the samples tested under $\sigma_0 \geq 35.12$ MPa, in which the curves for creep to the final failure as shown in Fig. 6. As shown in Fig. 7, for each stress level, the three groups of creep curves associated with the three creep stages are quite close, especially for the axial strain, which demonstrates once again that the samples employed in this research have good consistency and uniformity. From the above creep curves, the axial and lateral strains at the initial short-term loading (S0), the end of the transient stage (S1) and the onset of the accelerating stage (S2) can be readily obtained, as shown in Fig. 8. This figure shows that as the axial stress increases, the axial and lateral strains at S0 and S1 increase at different proportions, while the increases in the axial and lateral strains at S3 are quite small and almost negligible. Therefore, the strain differences between S0 and S1 as well as between S1 and S2, namely, the strains occurring during the transient and steady creep stages, are related to the magnitude of stress. Figure 9 shows the relationship between the average creep strains and axial stress in these two stages. Clearly, as the stress increases, the axial and lateral transient strains increase slightly, while the steady-state creep strain decreases sharply, with some local fluctuations.

According to the creep curves in Fig. 7, all the axial, lateral and volumetric critical strains at S2 for different stress levels are plotted in Fig. 10, and the corresponding average values are summarized in Table 3. The magnitudes of the three critical strains are relatively constant, approximately 0.65%, −0.42% and −0.2%, regardless of the stress level. This demonstrates that there is a critical damage threshold at the occurrence of the tertiary creep stage. Similar findings have also been reported in several previous experimental studies (Heap et al. 2009; Wang et al. 2020a, b). In addition, as can be further observed from Fig. 10, the magnitudes of the axial strains at S2 are almost comparable to those at the peak stress in the short-term uniaxial compression test, while the lateral and volumetric strains at S2 are slightly larger than those in the short-term test.

In addition to creep deformation, the steady creep rate and two critical creep time, namely, the time-to-onset of the accelerating stage t_{s2} and time-to-failure t_f, are of great importance for the prediction of engineering failure, especially in slope analysis. The steady creep rate refers to the strain rate at the secondary creep stage and is calculated from the slopes of the straight sections of creep curves.

Fig. 5 Stress–strain curves for the creep tests under different stress levels: **a** axial and lateral curves and **b** volume curves. Points C and D are the microcrack initiation point and the volumetric strain inflection point, respectively
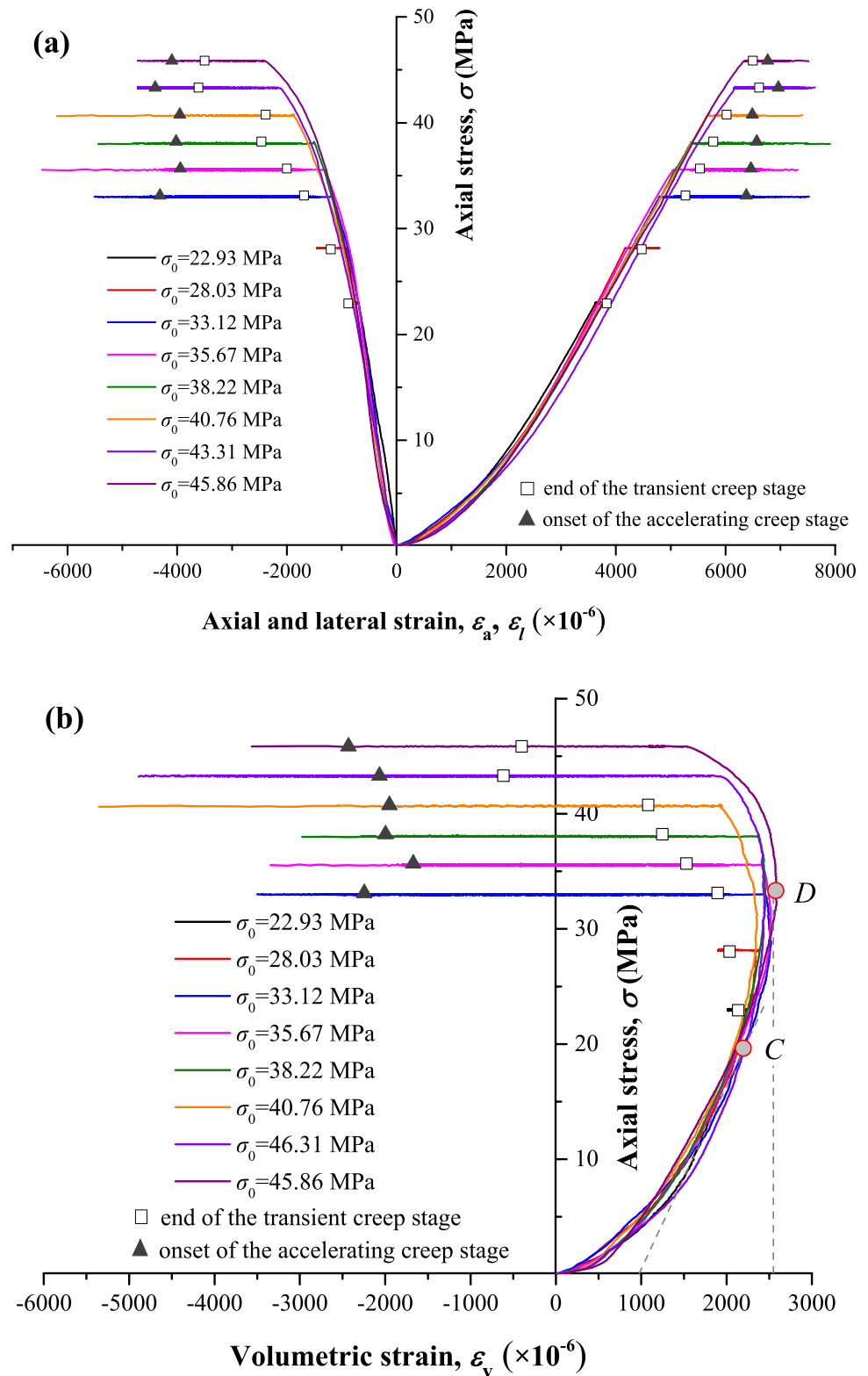

Table 3 summarizes all the axial and lateral steady creep rates for the different axial stress levels, and the relationship between them and the axial stress is plotted in Fig. 11. From Table 3, it is seen that both the axial and lateral steady

creep rates are extremely sensitive to the applied stress. Taking the axial strain rate as an example, at $\sigma_0 = 33.12$ MPa, the average steady creep rate is 1.6×10^{-7}/min, while as the stress increases to 45.86 MPa, steady creep rate increases to
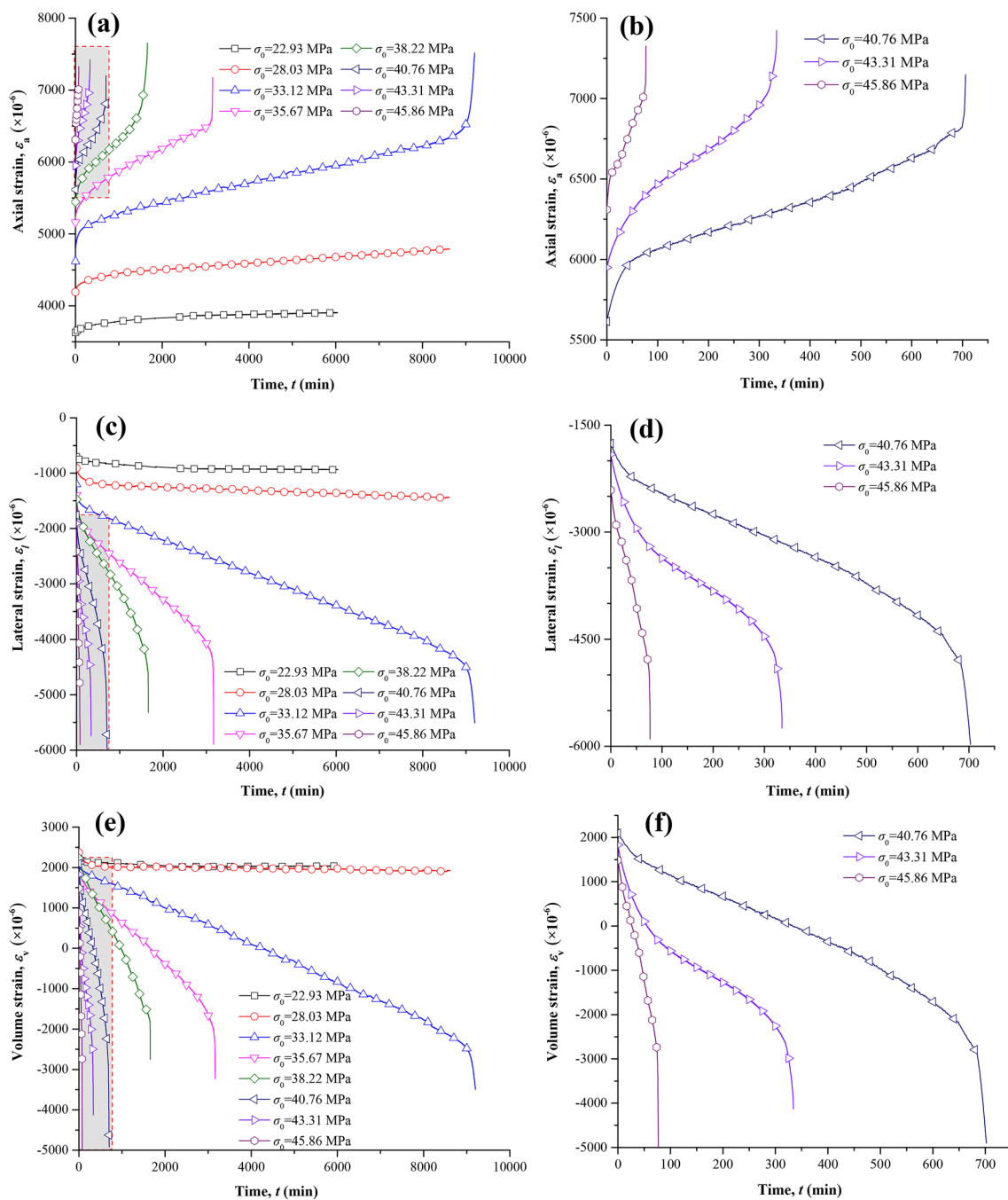
Fig. 6 Creep curves under different stress levels corresponding to Fig. 5: **a** and **b** axial strain, **c** and **d** lateral strain, and **e** and **f** volumetric strain; **b**, **d** and **f** are the local magnifications of **a**, **c** and **e**, respectively

1.98×10^{-5}/min. This implies that the increment of the stress of a few MPa induces an increment in the strain rate of up to several orders of magnitude. Furthermore, as shown in Fig. 11, the relationships of the creep strain rates in the axial and lateral directions with the stress also can be described well by the power law, i.e., axial strain rate $\dot{\varepsilon}_a = 4.09 \times 10^{-25} \sigma_0^{15.21}$ and lateral strain rate $\dot{\varepsilon}_l = 9.87 \times 10^{-28} \sigma_0^{17.08}$, which are fairly consistent with the findings from the creep tests

previously performed on other sandstones (Brantut et al., 2013; Yu et al., 2019). In addition, by comparing the slopes of the two fitted curves in Fig. 11, it is seen that the lateral creep strain rate is more sensitive to the stress level than the axial strain.

Table 3 lists the two creep times (t_{s2} and t_f) and their ratio (t_{s2}/t_f) for the samples in Fig. 6 that underwent creep to failure, and t_{s2} and t_f versus axial stress are
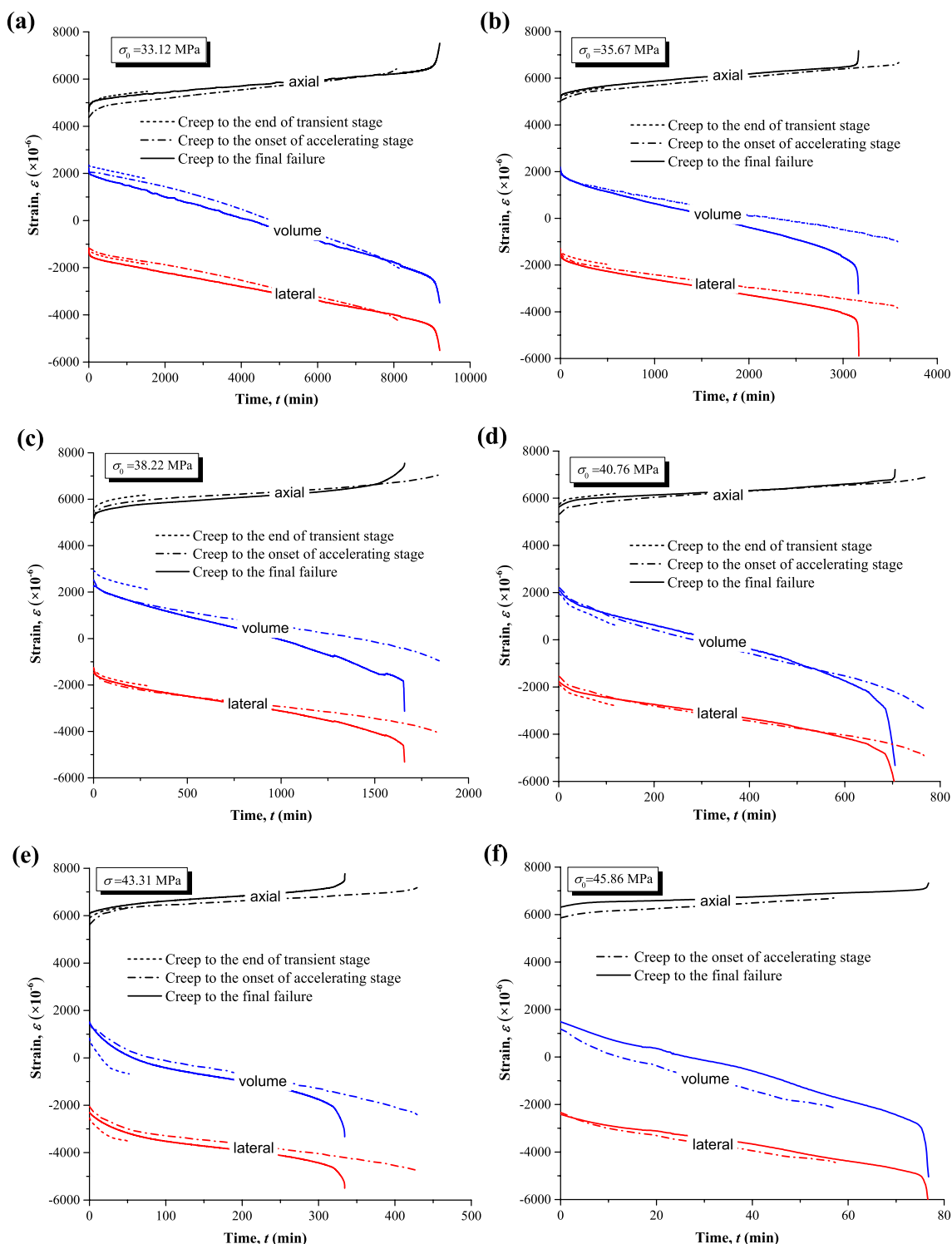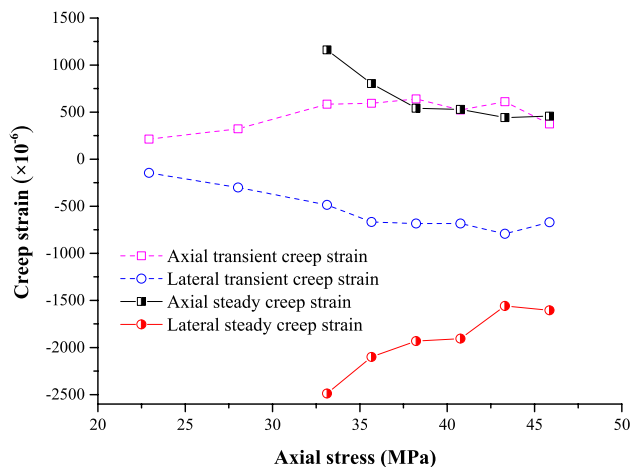
Fig. 7 Creep curves for all the samples that undergo creep to the three different stages under different stress levels: **a** $\sigma_0 = 33.12$ MPa, **b** $\sigma_0 = 35.67$ MPa, **c** $\sigma_0 = 38.22$ MPa, **d** $\sigma_0 = 40.76$ MPa, **e** $\sigma_0 = 43.31$ MPa, and **f** $\sigma_0 = 45.86$ MPa

also plotted in Fig. 12. Unlike the steady creep rates, as the axial stress increases, t_{s2} and t_f decrease sharply and t_{s2}/t_f decreases slightly, suggesting that under higher stresses, the creep duration is shorter, and the

accelerating creep occurs earlier. Moreover, as shown in Fig. 12, the relationships between the creep stress and two creep times can be well fitted with the exponential functions, namely, $t_{s2} = 3.55 \times 10^9 \exp(-0.39\sigma_0)$ and
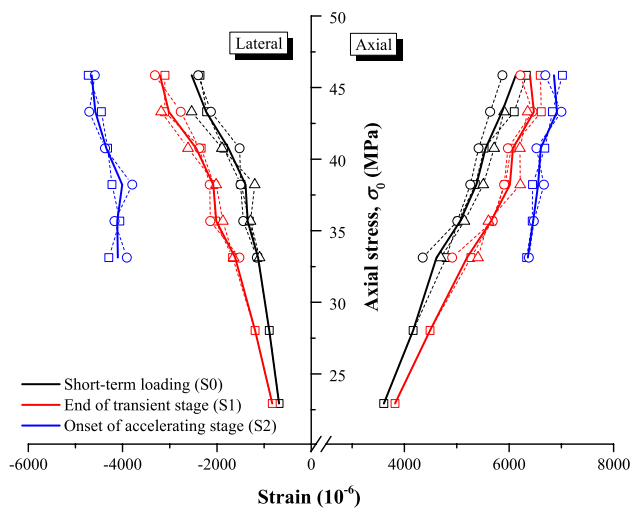
Fig. 8 Axial and lateral strains during the initial short-term loading (S0), the end of transient creep (S1) and the onset of accelerating creep (S2), where the symbols denote experimental data and the solid lines donate the corresponding average values
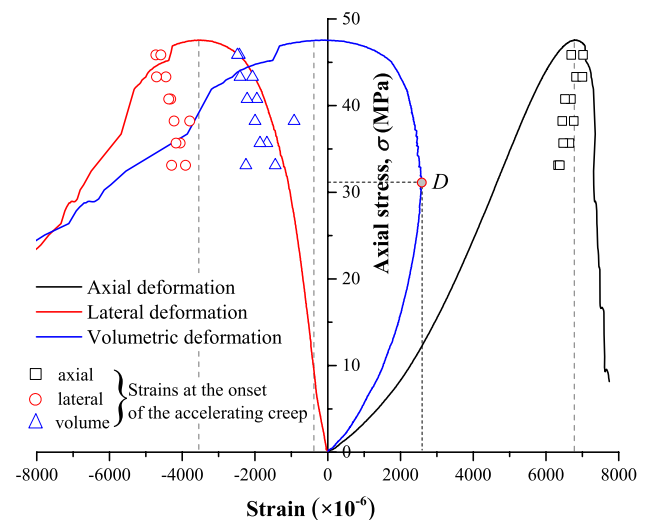

Fig. 10 Typical stress–strain curves for the uniaxial compression test, and the relative positions of the axial, lateral and volumetric strains at the onset of the accelerating creep stage

Fig. 9 Relationship between the axial and lateral transient and steady creep strains and axial stress

$t_f = 2.23 \times 10^9 \exp(-0.374\sigma_0)$. Similar fitting relationships have been proposed by Tang et al. (2018).

3.2 Pore Evolution Analysis

As mentioned in Experimental Methodology, the porosity and pore distribution of the samples after the mechanical tests were measured by NMR. However, with respect to pore evolution analysis, a key representative parameter of the rock pore structure, the T_2 cutoff, should be interpreted because it can reflect the degree of mobile fluid in porous media (Lyu et al. 2020). As specified in NMR theory, the pores in terms of T_2 less than the T_2 cutoff are generally

regarded as small pores, in which water is bound and difficult to displace; conversely, the pores with $T_2 > T_2$ cutoff are large pores, in which the water is free and mobile (Gao et al. 2019; Liu et al. 2018; Lu et al. 2020). In this study, the T_2 cutoff of the red sandstone measured by centrifugation is 3.9 ms (i.e., pore radius $r = 0.39$ μm). Hence, when a pore of the red sandstone are larger than 0.39 μm, it is regarded as a large pores, and a pore no larger than 0.39 μm is regarded as a small pore.

3.2.1 Moisture Migration in Pores During Loading

As mentioned in Experimental Methodology, to investigate the moisture migration law during mechanical loading, samples were tested by the NMR technique immediately after unloading. Here, we take the results of samples C5-1 and C5-3 as an example, which were subjected to short-term loading and creep loading at $\sigma_0 = 38.22$ MPa, respectively. Sample C5-3 underwent creep to the onset of the accelerating stage. Figure 13a and b show the NMR T_2 spectra of the two samples, where the Y-axis is the porosity component, corresponding to the signal intensity or amplitude used in the literature.

Figure 13 shows that the main changes in the porosity of the samples with different mechanical loadings are concentrated in the first two peaks. The initial T_2 spectra are somewhat different from those tested immediately after unloading. Whether a short-term test or a creep test was performed, during loading, the water content decreases in the large pores and increases in the small pores. However, the total water content in the sample during mechanical tests is almost constant since its surface was always tightly sealed

Table 3 Average strain at the onset of the accelerating creep stage, average steady creep rate and two creep times

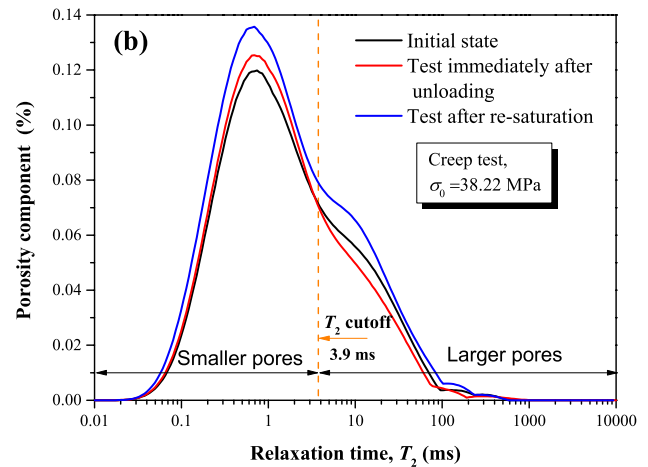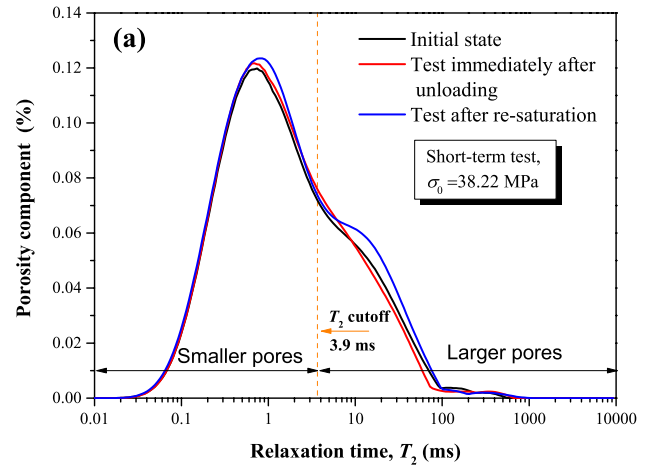| Stress σ_0 (MPa)	Strain at the onset of the accelerating creep stage (10^{-6})			Steady creep rate (min^{-1})		Time (min) and time ratio		
	Axial	Lateral	Volume	Axial	Lateral	t_{S2}	t_f	t_{S2}/t_f
33.12	6358	−4101	−1843	1.6×10^{-7}	3.2×10^{-7}	8621	9200	0.94
35.67	6460	−4114	−1768	3.1×10^{-7}	7.4×10^{-7}	2907	3161	0.92
38.22	6558	−4008	−1459	6.1×10^{-7}	1.26×10^{-6}	1409	1659	0.85
40.76	6605	−4344	−2084	1.24×10^{-6}	3.42×10^{-6}	578	706	0.82
43.31	6917	−4578	−2240	2.06×10^{-6}	5.57×10^{-6}	267	334	0.80
45.86	6857	−4657	−2456	1.98×10^{-5}	3.52×10^{-5}	44	68	0.79
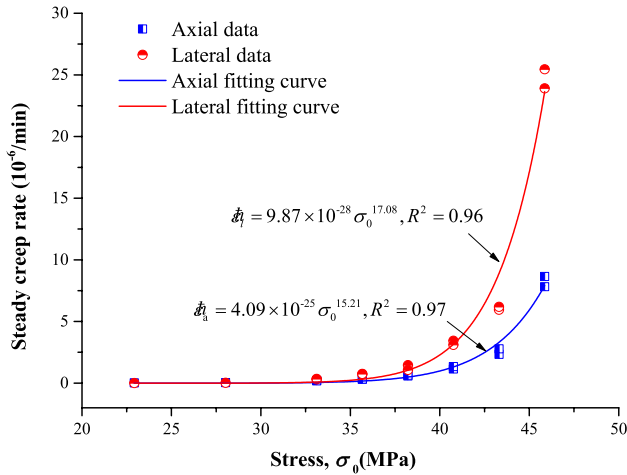
Fig. 11 Relationships between the axial and lateral steady creep rates and creep stress
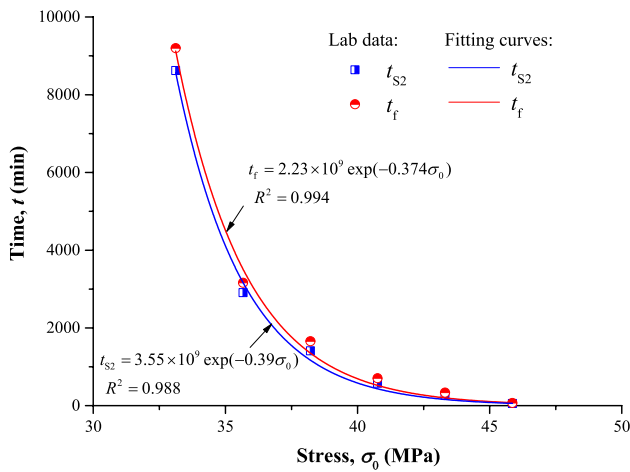
Fig. 12 Time to the secondary and tertiary creep stages under different constant creep stresses

Fig. 13 NMR T_2 distributions of two samples subjected to **a** short-term loading and **b** creep loading, at $\sigma_0 = 38.22$ MPa

by the waterproof membrane. Therefore, the water in the samples migrated progressively from the large pores into the smaller pores during loading. In particular, for the creep test, the change in porosity between the small pores and large pores is approximately 15.4%, which is much larger than the 4.2% observed in the short-term test. This indicates that the moisture migration in the creep test is more obvious than that in short-term loading. In addition, as observed in Fig. 11, after samples were resaturated, the areas of the T_2 spectrum were enlarged compared with the initial state,

and the increase in porosity during the creep test was also much larger than that during the short-term test. We further discuss this finding below.

### 3.2.2 Pore Evolution Under Different Creep Stresses

As previously mentioned, all samples after unloading were resaturated and retested by the NMR technique. According to the testing scheme, the T_2 spectra of all the samples under different stress levels and testing states are illustrated in Fig. 14. Here, the testing states are the initial state, after short-term loading (S0), after transient creep (S1), after transient and steady creep (S2), and after creep failure (S3). Moreover, each T_2 spectrum curve shown above is obtained from a single sample, which is in accordance with the creep curves in Fig. 7. However, as previously clarified, the heterogeneity between samples is small and thus does not impede the comparative analysis of the T_2 curves under different stress levels and different test states. In addition, during brittle failure, localized shear bands and macroscopic cracks usually appear in a sample, making it fracture into several parts. Therefore, in this study, NMR tests of the samples

after failure were performed on the relatively intact parts of the damaged samples.

Figure 14 shows that the overall shapes of the T_2 curves after the mechanical tests are essentially unchanged, with four peaks, similar to the initial unformed state. Based on the relationship between T_2 and the pore radius (see Eq. (1)), the pore radii for the four peaks approximately correspond to the intervals of 1–500 nm, 0.5–10.2 μm, 10.2–22 μm and 22–95 μm. In terms of each testing state, it is seen from Fig. 14a that the T_2 peak areas after short-term loading are all enlarged with increasing stress, whose main changes are concentrated near the first two peaks. Here, for clarity, the differences in the T_2 distribution between the initial state and after short-term loading for each stress level are shown in Fig. 15. The difference in the porosity components within the range of smaller pores ($T_2 < T_2$ cutoff) is apparently greater than that within the range of large pores ($T_2 > T_2$ cutoff), indicating that a larger number of small pores form during the short-term loading. Moreover, with the increase of the stress level, the increasing rate of total porosity increases sharply, indicating that the damage degree becomes more serious under the high loading ratio. The similar findings have also been observed by Cheng et al. (2021a, b).
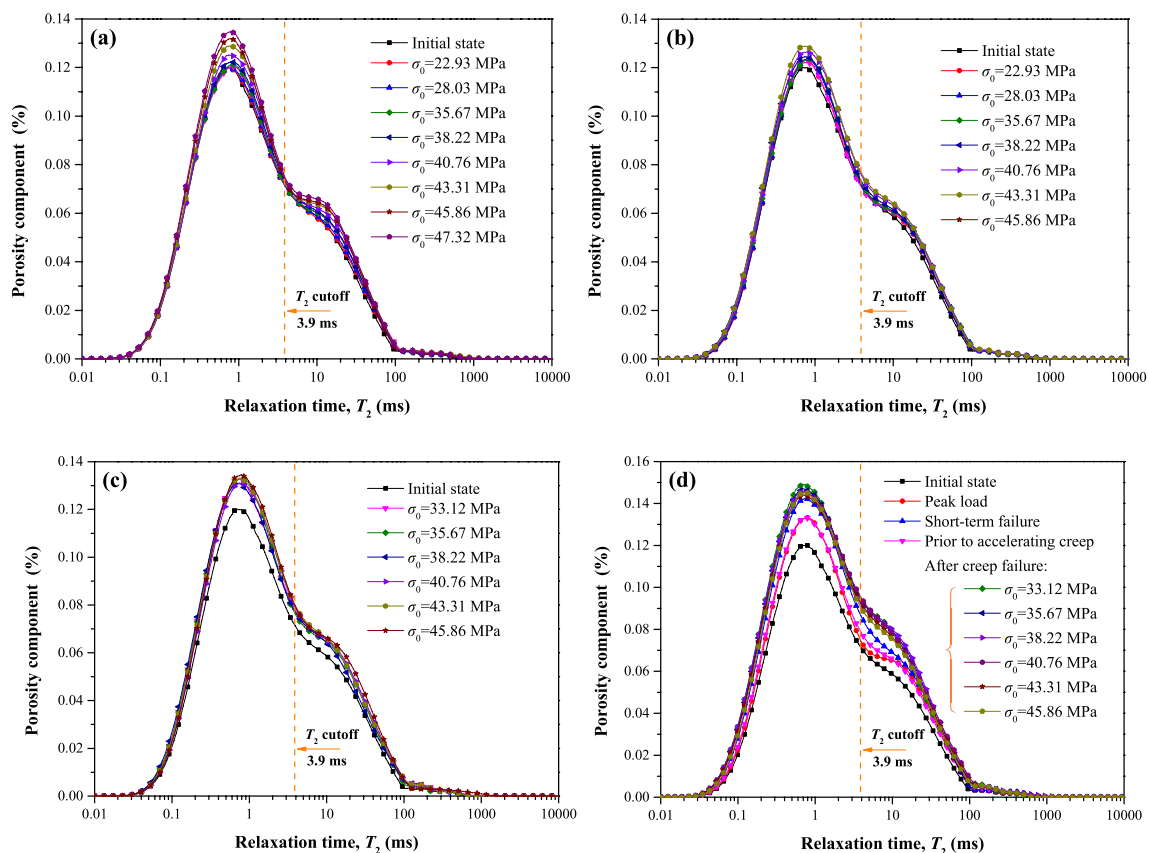
Fig. 14 T_2 relaxation distribution of samples under different axial stresses and at different testing states **a** after short-term loading, **b** after transient creep, **c** after transient and steady creep, and (d) after short-term and creep failure
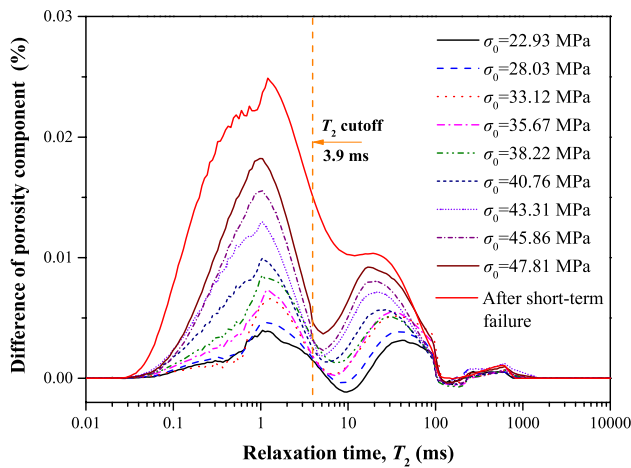
Fig. 15 Differences in the T_2 distributions with different stress levels between the initial state and that after short-term loading

Second, Fig. 14b and c show that the peak areas of the T_2 distribution after transient creep also gradually enlarge with increasing stress, while after transient and steady creep, the T_2 curves almost overlap with each other. Furthermore, as observed from Fig. 14d, all the peak areas of the T_2 curves after failure are substantially enlarged, especially after creep failure, and are much larger than those after short-term failure. However, under different stresses, the discrepancies between the curves after creep failure are small, especially at $T_2 > 40$ ms. By comparing the curve of the short-term peak load (i.e., $\sigma_0 = 48.32$ MPa) with that after short-term failure, it can be concluded that during the post peak damage stage, the proportion of small pores increases sharply, while the large pores, despite the increase, remain essentially unchanged at $T_2 > 20$ ms. In addition, Fig. 14d also presents the average pore size distribution for the samples taken to the onset of accelerating creep stage. Compared to the peak load, the two spectra are very close, especially

within the range of small pores. This indicates that the two critical states have a similar pore distribution. This is also basically in agreement with the results reflected in the creep strain above. However, this findings is not surprising since both states represent a point that is well into the expansion and cracking phase but prior to crack coalescence and damage localization (Brantut et al. 2013; Heap et al. 2009; Wu et al. 2000).

Corresponding to Fig. 14, the porosity of a sample under each stress level and testing state is obtained by accumulating the porosity components on the T_2 spectra. Table 4 lists the obtained porosity ϕ and the corresponding porosity difference $\Delta\phi$. Figure 16 shows the relationship between the porosity and axial stress for the samples after different stages of loading. Clearly, the porosities for samples S0 and S1 increase gradually with increasing axial stress. For a certain stress level, the differences in porosity (i.e., ϕ_{S1}-ϕ_{S0}) between the two testing states are fairly small, especially at
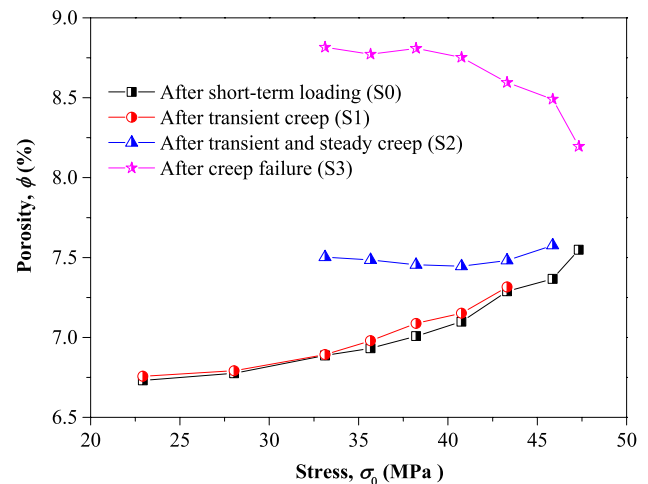
Fig. 16 Relationships between the porosity and axial stress at the four testing states

**Table 4** Porosity and porosity difference for various stages under different stress levels

Stress level σ_0 (MPa)	Porosity ϕ(%)				Porosity difference $\Delta\phi$(%)			
	ϕ_{S0}	ϕ_{S1}	ϕ_{S2}	ϕ_{S3}	ϕ_{S0}-ϕ_{Si}	ϕ_{S1}-ϕ_{S0}	ϕ_{S2}-ϕ_{S1}	ϕ_{S3}-ϕ_{S2}
22.93	6.74	6.76	–	–	0.04	0.02	–	–
28.03	6.78	6.79	–	–	0.08	0.01	–	–
33.12	6.88	6.91	7.52	8.82	0.18	0.02	0.61	1.30
35.67	6.93	6.99	7.48	8.77	0.23	0.06	0.49	1.29
38.22	7.01	7.07	7.45	8.81	0.31	0.06	0.38	1.36
40.76	7.11	7.18	7.47	8.75	0.41	0.07	0.33	1.28
43.31	7.25	7.35	7.49	8.60	0.59	0.10	0.14	1.12
45.86	7.37	–	7.53	8.49	0.67	–	–	0.96
47.87(peak load)	7.55	–	–	8.21	0.85	–	–	–

ϕ_{Si} Initial porosity, equal to 6.7%, ϕ_{S0} porosity after short-term loading, ϕ_{S1} porosity after transient creep, ϕ_{S2} porosity at the onset of the accelerating creep stage, and ϕ_{S2} porosity after failure

a lower axial stress. This indicates that the damage in the sample from S0 to S1 is not obvious. Meanwhile, in terms of the increasing gradient between every two subsequent stress levels, both curves at $\sigma_0 < 33.12$ MPa increase slowly, while for $\sigma_0 > 33.12$ MPa (0.7UCS), remarkable increases can be observed. This may be because unstable cracks between intergranular particles begin to form between grains begin and dislocate as σ_0 becomes larger than σ_D (Wen et al. 2018).

In addition, as observed from Table 4 and Fig. 16, the porosities for the samples after transient and steady creep (S2) are relatively constant and remain nearly unaffected by the stress. This again indicates that there is a critical damage state of the sample at the onset of accelerating creep and it occurs at a similar level in all cases. Moreover, the porosities of the samples after creep failure are substantially larger than those at S0, S1 and S2, and with increasing stress, the values tend to decrease (see Fig. 16). This demonstrates that the damage of the sample during the tertiary creep stage is more serious at a lower axial stress. The main reason for this result may be that when the stresses are lower, it takes longer to reach the final failure state, allowing more microcrack propagation before macroscopic shear bands or fractures form. A similar observation has been noticed by Brantut et al. (2014a, b), who indicated that a larger total strain arises at the final creep failure when the creep stresses are lower.

To further account for the porosity changes in different pore sizes, Fig. 17 shows the relationship of the porosity for the small and large pores with axial stress, where, as noted earlier, the small and large pores are demarcated by the T_2 cutoff. Comparing Figs. 16 and 17, it can be clearly observed that the changes in the two porosity components ϕ_s and ϕ_l with axial stress are basically the same as those of all the pores. Moreover, ϕ_s at each stress level is greater than ϕ_l.
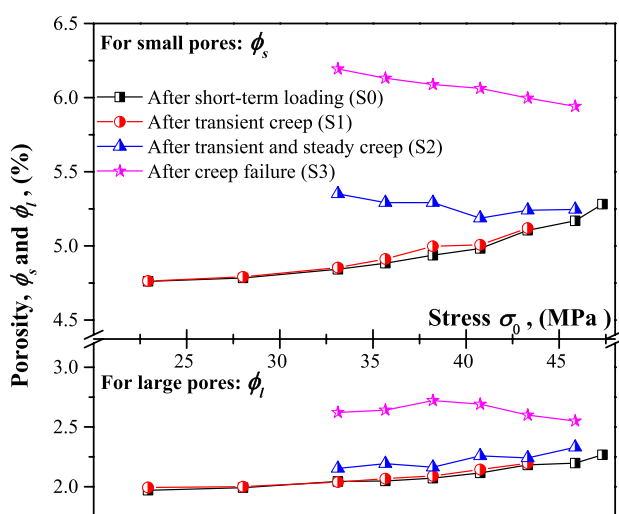

Fig. 17 Relationships between the porosity components (ϕ_s and ϕ_l) and the axial stress

3.2.3 Pore Evolution Under Different Creep Stages

To further investigate the pore evolution of different creep stages at a given stress level, corresponding to Fig. 14, Fig. 18 redraws the T_2 distribution of the samples under four test states of stress from $\sigma_0 = 33.12$–45.86 MPa. For each stress level, the peak area of the T_2 spectrum obviously increases throughout the testing process, which means that the porosity of the samples increases from short-term loading (S0) to long-term creep failure (S3). More specifically, to quantitatively evaluate the T_2 spectrum changes of the samples after loading for different durations, taking $\sigma_0 = 40.76$ MPa as an example (see Fig. 18f), the differences in the T_2 spectra for samples between the initial state and after the four-stage mechanical tests are plotted in Fig. 19a. After the four-stage mechanical tests, the curves of the difference in porosity component remain basically above zero, indicating that the porosity components corresponding to different T_2 increase, especially within the range of 0.1–100 ms. However, along the T_2 axis, the above curves show obvious fluctuations, indicating that the increments in the porosity component at each pore size are quite different. By comparing the four test states, it can be seen that the above curves of S0, S1 and S2 show a similar trend but substantially differ from that after creep failure, whose peak area is much larger than those of other three curves.

In this regard, as shown in Fig. 19b, the porosity increments for the small and large pores in the sample after the four-stage tests are determined. The porosity increments of the two kinds of pores increase gradually from S0 to S3, and for each testing state, the increment corresponding to the small pores is substantially larger than that of the large pores. This is consistent with the observation obtained by Cheng et al. (2021a, b), although the samples in their study only experienced transient creep or partial steady-state creep. Furthermore, the total porosity increment for all the pores increases with the testing states as well, increasing by 0.39%, 0.52%, 0.77% and 2.05%, respectively. Clearly, the difference in the porosity increment between S0 and S1 is not significant and is much smaller than that between S1 and S2. However, the porosity increment after creep failure (S3) is much greater than the earlier states. More specifically, from Table 4, we can observed that the average total porosities for all the samples taken to S2 and S3 are 7.49% and 8.71%, respectively. Correspondingly, the percentage increases relative to the initial porosity are 11.8% and 29.8%, respectively. Clearly, the porosity increment at S3 is almost 2.5-fold that at S2. Moreover, in the increased porosities, the porosity of the small pores account for a large proportion: 60% for S2 and 62% for S3. Above results indicate that the total porosity increases sharply from the onset of the accelerating stage to final creep failure, especially the proportion contributed by the small pores.
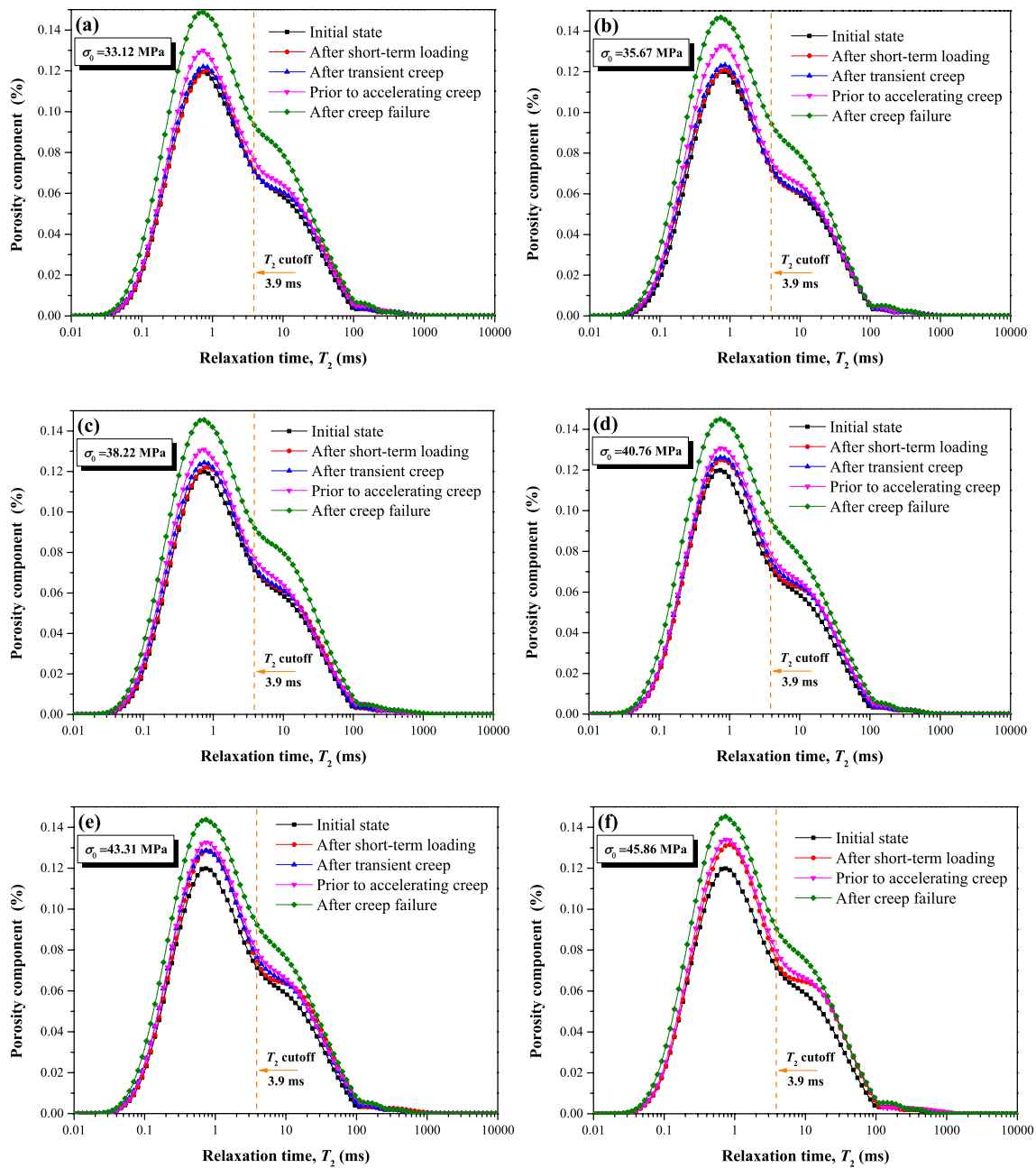
Fig. 18 NMR T_2 distribution of the samples at different testing states and stress levels, where **a**–**f** correspond to the eight stress levels listed in Table 2

In addition, comparing the closest stress level between Cheng et al. (2021a, b) and ours (i.e., the creep stress is about 0.8UCS), the maximum porosity increment in their work is about 0.386%, which is significantly less than the 0.75% at S2 in our tests, but slightly larger than 0.37% at S1 (see $\sigma_0 = 38.22$ MPa in Table 4). The difference may be due to three main factors: first, the pore size distribution and the initial porosity of the sandstones in the two studies are different. Second, the samples in Cheng's test were unsaturated, so the creep effect would be generally smaller (Deng et al. 2016; Yu et al. 2019). Third, the duration of creep in Cheng's work seems insufficient for samples to undergo creep to the onset of the accelerating stage. Therefore, at the same stress level, we obtain a significantly larger porosity increment than theirs.

3.3 Microstructural Observations

Corresponding to the pore evolution analysis, microstructural observations with SEM are further conducted.
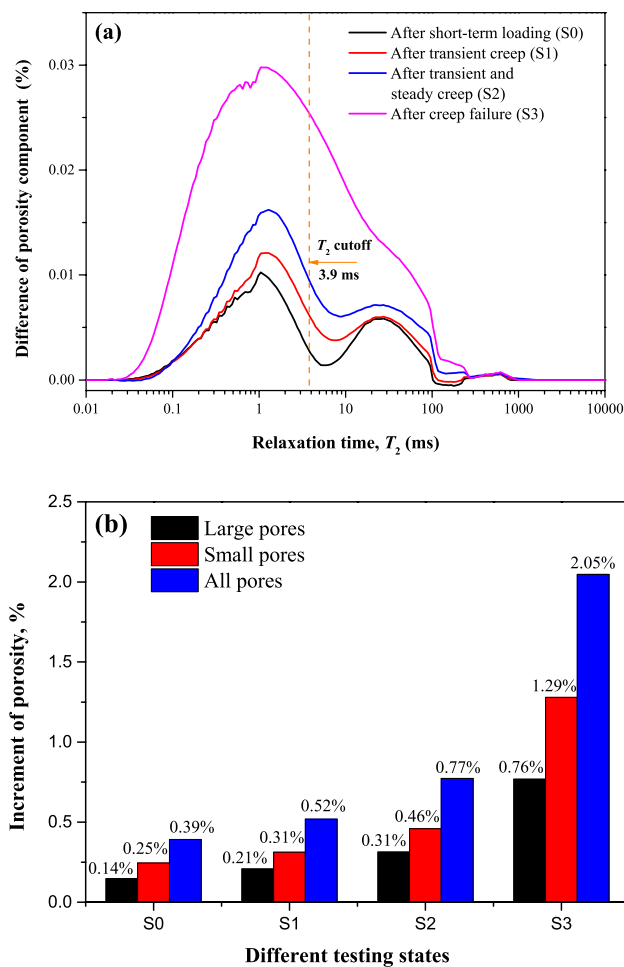
Fig. 19 For $\sigma_0 = 40.76$ MPa, **a** differences in the T_2 distribution between the initial state and after the four-stage tests, and **b** the corresponding porosity increments during the four-stage mechanical tests

Figure 20 shows the SEM images of the three samples after experiencing creep to S1, S2 and S3, where the microcracks along the grain boundaries are intergranular crack and within the grains are transgranular crack. As noted earlier, the minimum pore size of this sandstone is greater than 5 nm. Therefore, by comparing Fig. 20 with Fig. 19, it can be seen that the porosity of the sample is mainly contributed by the intergranular cracks and micropores. Considering Fig. 20 a, c and e, we can see that the connection between crystal granules inside the samples becomes looser as the samples creep from S1 to S3. Specifically, as shown in Fig. 20a and b, after transient creep, the intergranular connections in the sample are still tight, similar to the initial unformed state (see Fig. 1), with only some localized intergranular loosening. In contrast, for the sample after transient and steady creep (see Fig. 20c and d), the intergranular loosening is more pronounced and small amounts of crystal grains with lower strength, such as feldspar and clay, begin to break. However, after the sample fails (see Fig. 20e and f),

widespread loosening of the connections at the intergranular boundaries can be observed, and with the coalescence of intergranular cracks, large numbers of macrocracks appear in the sample. Similar observations were noted by Heap et al. (2009) from optical photomicrographs of DDS sandstone as well. Therefore, it can be concluded that the brittle creep of the sandstone is driven by microscopic subcritical crack growth within granules and along granular boundaries, and that the increase in porosity is mainly due to the latter. This is remarkably different from ductile creep in porous rocks, where a large number of large particles are crushed, resulting in the pore space to collapse and small particles to slide into the pore space (Brantut et al. 2014a, b; Heap et al. 2015; Wong and Baud 2012).

4 Discussion

Within the framework of damage theory, damage is generally considered to be the formation of pore space (including pores and cracks) inside rock samples (Abdallah et al. 2021; Weng et al. 2018; Zheng et al. 2016). In classical damage analysis, irreversible strain or irreversible work is often used to evaluate the degree of damage in samples (Amitrano and Helmstetter 2006; Baud and Meredith 1997; Liu and Dai 2018). However, with the application of NMR, porosity is also regarded as an effective indicator to evaluate the damage in samples (Li et al. 2019; Weng et al. 2019; Zhou et al. 2018a, b). Therefore, based on the NMR testing results, the relationships between the irreversible strain and porosity increment for the samples after mechanical tests can be established. Meanwhile, the creep damage associated with different creep loadings can be quantitatively analyzed and discussed in combination with porosity.

To characterize rock creep deformation, numerous creep damage constitutive models have been proposed in previous works (Cheng et al. 2021a, b; Fahimifar et al. 2015; Ma et al. 2012; Wang and Cai 2020; Wang et al. 2019; Yang et al. 2014a, b). However, in this study a nonlinear elasto-viscoplastic creep constitutive model proposed by Zhao et al. (2018) is employed (see Fig. 21), taking into account its advantage in separating out the different strain components. In this model, the total strain consists of the following four components: instantaneous elastic strain, instantaneous plastic strain, viscoelastic strain, and viscoplastic strain. To describe the three stages of creep, the Kachanov creep damage law is adopted to account for the weakening of the viscoplastic viscosity coefficient with time, namely, $\eta_{vp2}(t) = \eta_0(1-\omega)$, where ω is the creep damage variable and η_0 is the initial viscosity coefficient. At the beginning of creep (i.e., at $t=0$), $\omega=0$, while at creep failure (at $t=t_f$), $\omega=1$. Furthermore, under an axial stress σ_0, the one-dimensional creep equation of this model is given as follows:

Fig. 20 SEM images of the samples after being subjected to different creep stages at $\sigma_0 = 40.76$ MPa, **a** and **b** after transient creep, **c** and **d** after transient and steady creep, and **e** and **f** after creep failure. **b**, **d** and **f** are the magnified images of the rectangles shown in **a**, **c** and **e**
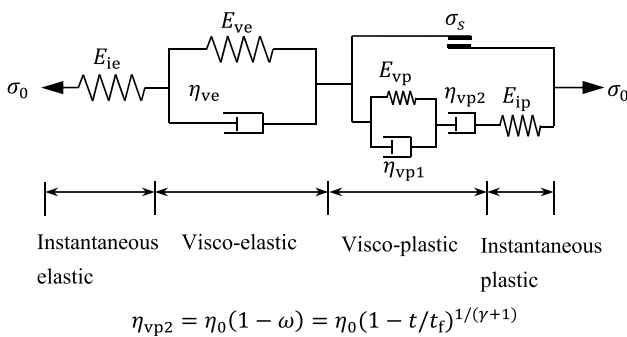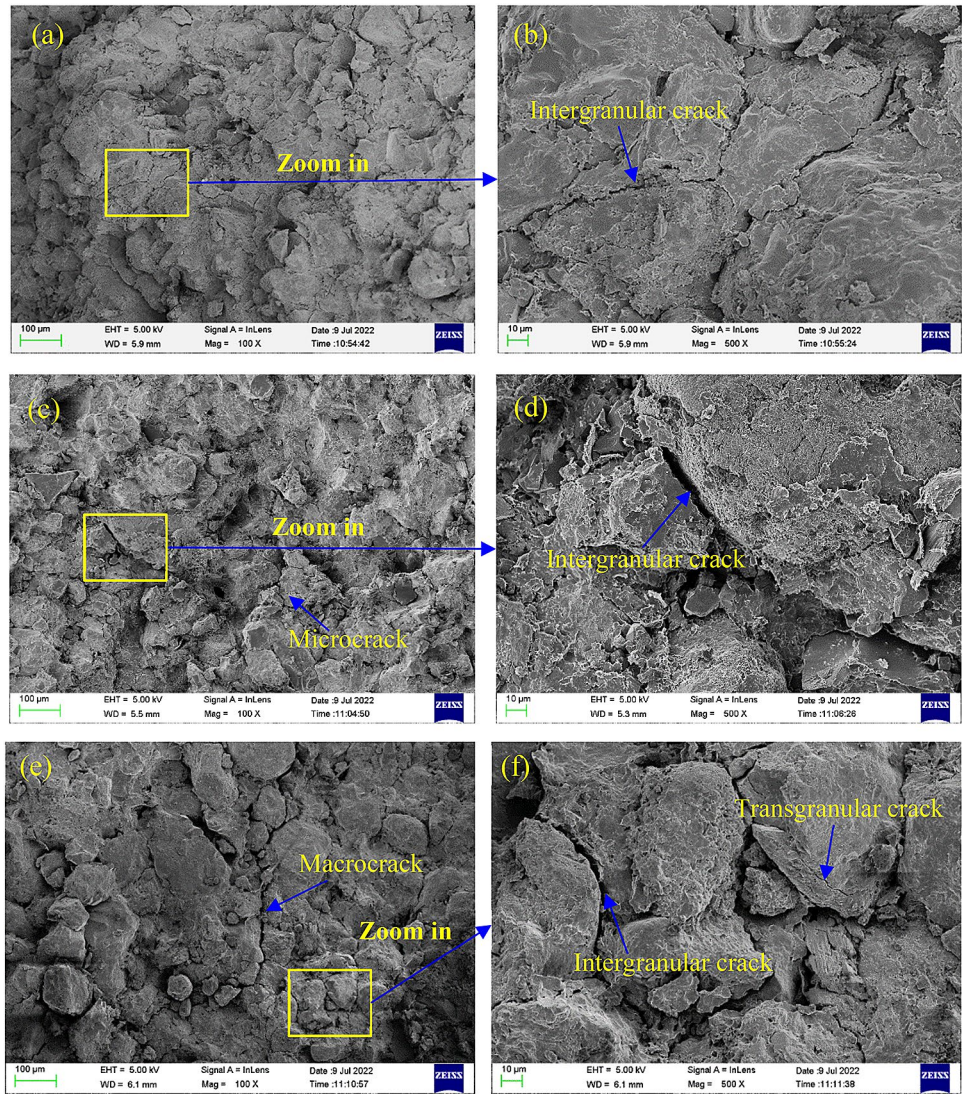

Fig. 21 EVP creep model proposed by Zhao et al. (2018)

$$\varepsilon_a(t) = \frac{\sigma_0}{E_{ie}} + \left(\frac{\sigma_0}{kE_{vp}} + \frac{\sigma_0 - \sigma_s}{E_{vp}} \right) \left[1 - \exp\left(-\frac{E_{vp}t}{\eta_{vp1}} \right) \right] + \frac{\sigma_0 - \sigma_s}{E_{ip}},$$
$$+ \frac{(\sigma_0 - \sigma_s)t_f(\gamma + 1)}{\eta_0\gamma} \left[1 - \left(1 - \frac{t}{t_f} \right)^{\gamma/(\gamma+1)} \right]$$

$$(2)$$

where ε_a is the axial strain; E_{ie} is the instantaneous elastic parameter; E_{ip} is the instantaneous plastic parameter; E_{ve} and η_{ve} are the viscoelastic parameters; E_{vp} and η_{vp1} are the viscoplastic parameters; σ_s is the long-term strength; t_f is the time-to-failure at a constant stress level; γ is the material constant related with the damage variable ω; and k is the constant factor to account for the simplified relationship between the viscoelastic parameters and viscoplastic parameters, i.e., $E_{ve} = kE_{vp}$ and $\eta_{ve} = k\eta_{vp1}$. Detailed descriptions of the above parameters are given in Zhao et al. (2018).
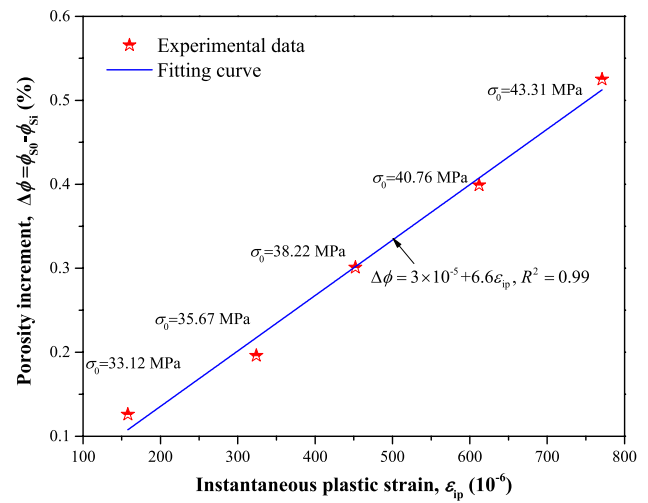
To analyze the whole process of damage in the three stages of creep, as shown in Fig. 22, the samples that
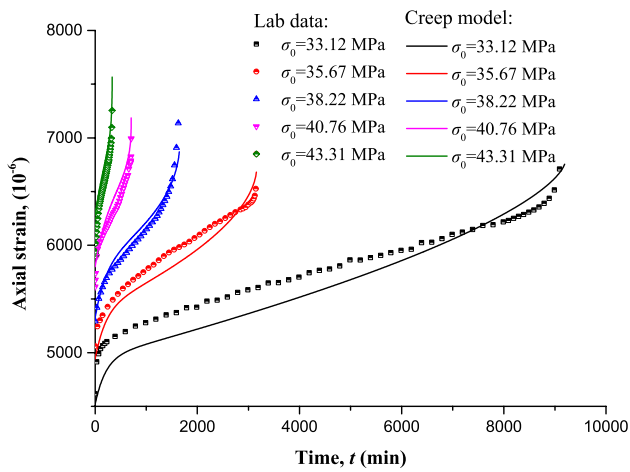
Fig. 22 Comparison between the experimental data and EVP creep model prediction at five different levels of axial stress

Fig. 23 Relationship between the instantaneous plastic strain and porosity increment resulting from short-term loading

underwent creep to the final failure under five stress levels are chosen for analysis in this study. Based on the above creep model, the experimental data are all fitted (see Fig. 22), and the corresponding model parameters are obtained as follows: $E_{ie} = 7.75$ GPa, $E_{ve} = 65.33$ GPa, $\eta_{ve} = 4.35 \times 10^4$ GPa·min, $E_{ip} = 27.56$ GPa, $E_{vp} = 217.76$ GPa, $\eta_{vp1} = 14.5 \times 10^4$ GPa·min, $\eta_0 = 1.28 \times 10^4$ GPa·min, $\sigma_s = 20.8$ MPa, $k = 0.3$ and $\gamma = 1.23$. Figure 22 shows that the predictions with the EVP model are in good agreement with the experimental data, indicating that the creep model can accurately describe the creep behavior of the samples. According to the fitting results, the calculated elastic, plastic, viscoelastic, and viscoplastic strains at the onset of accelerating creep stage at each stress level are shown in Table 5.

As noted above, both porosity and irreversible strain can be used to evaluate the damage of a sample. Therefore, after short-term loading, as shown in Fig. 23, a notable positive correlation between the porosity increment ϕ_{S0}-ϕ_{Si} and instantaneous plastic strain can be observed, and with increasing stress, both quantities increase dramatically, indicating that the damage degree increases as well. Meanwhile, with the fitted experimental data, a linear function can be

used to describe the above relationship, which is expressed as:

$$\Delta\phi = 3 \times 10^{-5} + 6.6\varepsilon_{ip}, \; R^2 = 0.99, \tag{3}$$

where $\Delta\phi = \phi_{S0}$-ϕ_{Si}, (%) and ε_{ip} is the instantaneous plastic strain (10^{-6}).

Similarly, Fig. 24 shows the relationship between the viscoplastic strain and porosity increment ϕ_{S2}-ϕ_{S0} at the onset of the accelerating creep stage. However, different from plastic strain, the two quantities decrease sharply as the stress increases since the total strain and porosity at S2 in all cases are basically identical, as discussed previously. Likewise, the relationship between the two quantities also shows a good positive linear correlation, namely:

$$\Delta\phi = 0.0019 + 4.23\varepsilon_{vp}, \; R^2 = 0.98, \tag{4}$$

where $\Delta\phi = \phi_{S2}$-ϕ_{S0}, (%) and ε_{vp} is viscoplastic strain, (10^{-6}).

Furthermore, based on the above fits and the porosity results in Table 5, the creep damage variable ω_{s2} and the

Table 5 Axial strain composition at the onset of the accelerating creep stage

Stress level σ_0 (MPa)	ε_{ie} (10^{-6})	ε_{ip} (10^{-6})	ε_{ve} (10^{-6})	ε_{vp} (1^{-6})	ε_{tot_cal} (10^{-6})	ε_{tot_mea} (10^{-6})
33.12	4407	158	388	1307	6260	6380
35.67	4637	324	412	1100	6473	6264
38.22	4900	452	441	651	6444	6569
40.76	5226	612	470	366	6674	6488
43.31	5553	771	500	185	7009	6762

ε_{ie} instantaneous elastic strain, ε_{ip} instantaneous plastic strain, ε_{ve} viscoelastic strain, ε_{vp} viscoplastic strain, ε_{tot_cal} calculated total strain, and ε_{tot_mea} measured total strain
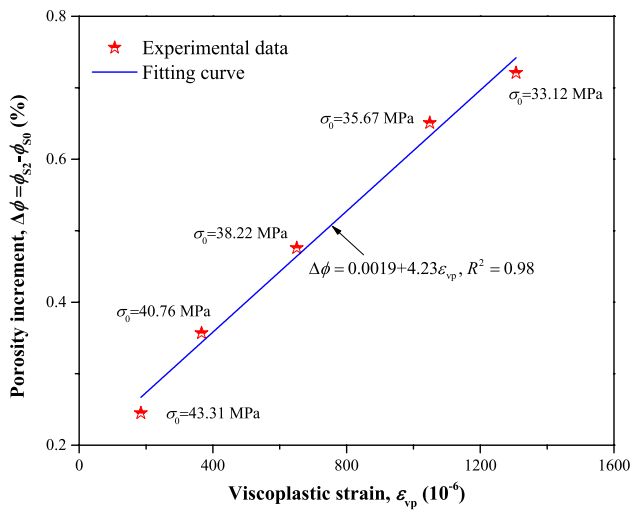
Fig. 24 Relationship between the viscoplastic strain and porosity increment at the onset of the accelerating creep stage
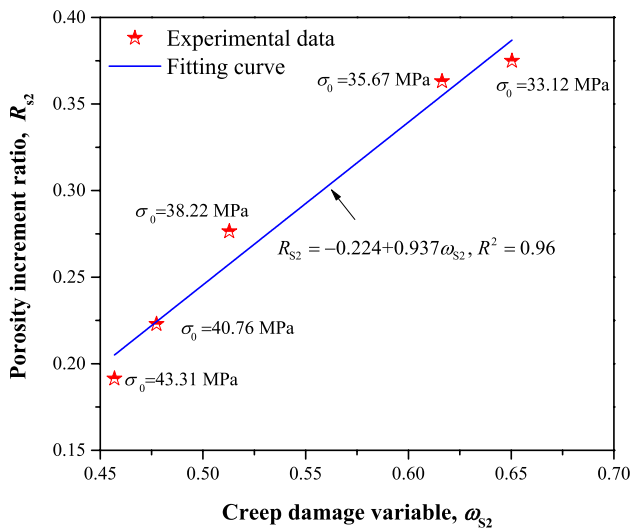
Fig. 25 Relationship between the creep damage variable ω_{S2} and the porosity increment ratio R_{S2} at the onset of the accelerating creep stage

porosity increment ratio R_{S2} at the onset of the accelerating creep stage are obtained, and the relationship between them is shown in Fig. 25. Here, $R_{S2} = (\phi_{S2}-\phi_{S0})/(\phi_{S3}-\phi_{S0})$, which is the increment ratio of the porosity occurring in the primary and secondary creep stages to that occurring in the entire creep process. Clearly, when $\phi_{S2} = \phi_{S0}$, R_{S2} equals zero, and when $\phi_{S2} = \phi_{S3}$, R_{S2} equals one. Accordingly, R_{S2} reflects the creep damage at S2, similar to ω_{S2}. R_{S2} is slightly smaller than ω_{S2}, which may be due to the fitting error of the EVP creep model and the limitation of the porosity index. Nevertheless, the relationship between the two quantities also can be described by the following linear equation.

$$R_{S2} = -0.224 + 0.937\omega_{S2}, \ R^2 = 0.96 \tag{5}$$

In addition, ω_{s2} and R_{s2} decrease with increasing stress, indicating that less creep damage occurs during S0 to S2 at higher stresses. This is intuitive, since the instantaneous damage induced by loading is greater at a higher stress, whereas the total damage at the onset of tertiary creep is consistent among all the cases studied. Generally, it can be concluded from the above analysis that the change in the porosity of the rock samples is directly related to the creep damage process and that the porosity increment is a reliable indicator for evaluating the degree of rock damage.

5 Conclusion

In this study, a series of mechanical and NMR tests were carried out to explore the microcracking and pore evolution of saturated red sandstone during short-term loading and long-term creep under axial compression. Based on the experimental results, the following conclusions can be drawn.

(1) As the stress increases, the axial and lateral transient creep strains increase slightly, while the steady creep strain drops sharply, albeit with some local fluctuations. The magnitudes of the axial and lateral critical strains at the onset of the accelerating creep stage are both relatively constant regardless of the stress level, and the axial critical strain is almost comparable to that at the peak stress in the short-term test, while the lateral critical strain is larger than that of the short-term test. Both the axial and lateral steady creep rates are extremely sensitive to the applied stress, and an increase of a few megapascals leads to an increase in the strain rate by up to several orders of magnitude. Conversely, as the stress increases, the two critical creep times (i.e., the time-to-onset of accelerating stage and the time-to-failure) decrease sharply, and the relationships between them and stresses can be described by the negative power law and the exponential law, respectively.

(2) During mechanical loading, the moisture migrates from the large pores (> 0.39 μm) into the small pores (< 0.39 μm) in the sample, and this phenomenon is more obvious in the creep test than in the short-term test for the same stress level.

(3) After the short-term and creep mechanical tests, the overall shape of the NMR T_2 spectrum of a sample is basically the same as the initial state, but the corresponding T_2 peak area and porosity both increase with the stress level. During the two mechanical tests, the increasing proportion of the small pores within the samples is much greater than that of the large pores. Regarding the three creep stages, the porosity increment caused by the transient stage is very small, while those caused by both the steady stage and

accelerating stage are closely dependent on the stress level, and the higher the stress level is, the smaller the corresponding porosity increments both are. However, regardless of the stress level, the porosity of the sample at the onset of the accelerating stage is always relatively constant, indicating that the onset of the accelerating stage corresponds to a critical damage state of the sample. In addition, compared to the initial porosity of 6.7%, the average porosities of samples taken to the onset of the tertiary stage and creep failure is 7.49% and 8.71%, i.e., the percentages increases are 11.8% and 29.8%, respectively. The average total porosity increment at S3 is almost 2.5-fold that at S2.

(4) SEM analysis shows that the brittle creep of sandstone is mainly driven by microscopic subcritical crack growth within grains and along granular boundaries. The increase in the porosity of the samples is mainly caused by this microcracking.

(5) The creep damage analysis based on porosity shows that increases in the porosity and the irreversible plastic and viscoplastic strains satisfy good linear relationships at all stress levels. The porosity increment is a reliable indicator for evaluating the degree of creep damage.

Data Availability All data generated during the study are available from the corresponding author by request.

Declarations

Conflict of interest The authors declare that they have no conflicts of interest.

References

Abdallah Y, Sulem J, Bornert M, Ghabezloo S, Stefanou I (2021) Compaction banding in high-porosity carbonate rocks: 1. experimental observations. J Geophys Res 126(1):e2020JB020538. https://doi.org/10.1029/2020JB020538

Amitrano D, Helmstetter A (2006) Brittle creep, damage, and time to failure in rocks. J Geophys Res. https://doi.org/10.1029/2005JB004252

Ashby MF, Sammis CG (1990) The damage mechanics of brittle solids in compression. Pure Appl Geophys 133(3):12. https://doi.org/10.1007/bf00878002

Baud P, Meredith PG (1997) Damage accumulation during triaxial creep of darley dale sandstone from pore volumometry and acoustic emission. Int J Rock Mech Min Sci 34(3):24.e21-24.e10. https://doi.org/10.1016/S1365-1609(97)00060-9

Brantut N, Baud P, Heap MJ, Meredith PG (2012) Micromechanics of brittle creep in rocks. Geophys Res 117(B8):12. https://doi.org/10.1029/2012JB009299

Brantut N, Heap MJ, Meredith PG, Baud P (2013) Time-dependent cracking and brittle creep in crustal rocks: a review. J Struct Geol 52:17–43. https://doi.org/10.1016/j.jsg.2013.03.007

Brantut N, Heap MJ, Baud P, Meredith PG (2014a) Mechanisms of time-dependent deformation in porous limestone. J Geophys Res 119(7):5444–5463. https://doi.org/10.1002/2014JB011186

Brantut N, Heap MJ, Baud P, Meredith PG (2014b) Rate- and strain-dependent brittle deformation of rocks. J Geophys Res 119(3):1818–1836. https://doi.org/10.1002/2013JB010448

Cai C, Li G, Huang Z, Shen Z, Tian S, Wei J (2014) Experimental study of the effect of liquid nitrogen cooling on rock pore structure. J Nat Gas Sci Eng 21:507–517. https://doi.org/10.1016/j.jngse.2014.08.026

Cao Y, Deng J, Yu B, Tan Q, Ma C (2014) Analysis of sandstone creep and wellbore instability prevention. J Nat Gas Sci Eng 19:237–243. https://doi.org/10.1016/j.jngse.2014.05.013

Chandler NA (2013) Quantifying long-term strength and rock damage properties from plots of shear strain versus volume strain. Int J Rock Mech Min Sci 59:105–110. https://doi.org/10.1016/j.ijrmms.2012.12.006

Charles RJ (1958) Static fatigue of glass. J Appl Phys 29(11):4

Chen M, Dai J, Liu X, Qin M, Pei Y, Wang Z (2018) Differences in the fluid characteristics between spontaneous imbibition and drainage in tight sandstone cores from nuclear magnetic resonance. Energy Fuels 32(10):10333–10343. https://doi.org/10.1021/acs.energyfuels.8b01396

Cheng H, Zhang Y, Zhou X (2021a) A nonlinear creep model for rocks considering damage evolution based on the modified Nishihara model. Int J Geomech. https://doi.org/10.1061/(ASCE)GM.1943-5622.0002071

Cheng H, Zhou X, Pan X, Berto F (2021b) Damage analysis of sandstone during the creep stage under the different levels of uniaxial stress using NMR measurements. Fatigue Fract Eng Mater Struct 44(3):719–732. https://doi.org/10.1111/ffe.13389

Chu Z, Wu Z, Liu Q, Liu B, Sun J (2021) Analytical solution for lined circular tunnels in deep viscoelastic burgers rock considering the longitudinal discontinuous excavation and sequential installation of liners. J Eng Mech. https://doi.org/10.1061/(ASCE)EM.1943-7889.0001912

Cong Y, Wang Z, Zheng Y, Zhang L (2020) Effect of unloading stress levels on macro- and microfracture mechanisms in brittle rocks. Int J Geomech 20(6):04020066. https://doi.org/10.1061/(ASCE)GM.1943-5622.0001647

Costin LS (1983) A microcrack model for the deformation and failure of brittle rock. J Geophys Res 88(B11):9485–9492. https://doi.org/10.1029/JB088iB11p09485

Deng HF, Zhou ML, Li JL, Sun XS, Huang YL (2016) Creep degradation mechanism by water-rock interaction in the red-layer soft rock. Arab J Geosci. https://doi.org/10.1007/s12517-016-2604-6

Fahimifar A, Karami M, Fahimifar A (2015) Modifications to an elasto-visco-plastic constitutive model for prediction of creep deformation of rock samples. Soils Found 55(6):1364–1371. https://doi.org/10.1016/j.sandf.2015.10.003

Fan LF, Gao JW, Wu ZJ, Yang SQ, Ma GW (2018) An investigation of thermal effects on micro-properties of granite by X-ray CT technique. Appl Therm Eng 140:505–519. https://doi.org/10.1016/j.applthermaleng.2018.05.074

Fan L, Gao J, Du X, Wu Z (2020) Spatial gradient distributions of thermal shock-induced damage to granite. J Rock Mech Geotech Eng 12(5):917–926. https://doi.org/10.1016/j.jrmge.2020.05.004

Gao F, Wang Q, Deng H, Zhang J, Tian W, Ke B (2017) Coupled effects of chemical environments and freeze–thaw cycles on damage characteristics of red sandstone. Bull Eng Geol Env 76(4):1481–1490. https://doi.org/10.1007/s10064-016-0908-0

Gao H, Wang C, Cao J, He M, Dou L (2019) Quantitative study on the stress sensitivity of pores in tight sandstone reservoirs of Ordos basin using NMR technique. J Petrol Sci Eng 172:401–410. https://doi.org/10.1016/j.petrol.2018.09.083

Guayacán-Carrillo L-M, Sulem J, Seyedi DM, Ghabezloo S, Armand G (2018) Size effect on the time-dependent closure of drifts in Callovo-Oxfordian claystone. Int J Geomech 18(10):04018128. https://doi.org/10.1061/(ASCE)GM.1943-5622.0001213

Hao L, Zuliang Z, Imo-Imo EK, Yong S, Xinrong L, Dongmin Y (2020) Experimental investigation of the permeability and mechanical behaviours of chemically corroded limestone under different unloading conditions. Rock Mech Rock Eng 53(4):1587–1603. https://doi.org/10.1007/s00603-019-01961-y

Heap MJ, Baud P, Meredith PG, Bell AF, Main IG (2009) Time-dependent brittle creep in Darley Dale sandstone. J Geophys Res. https://doi.org/10.1029/2008JB006212

Heap MJ, Brantut N, Baud P, Meredith PG (2015) Time-dependent compaction band formation in sandstone. J Geophys Res 120(7):4808–4830. https://doi.org/10.1002/2015JB012022

Li XZ, Shao ZS (2016) Micro–macro modeling of brittle creep and progressive failure subjected to compressive loading in rock. Environ Earth Sci 75(7):583. https://doi.org/10.1007/s12665-016-5365-3

Li J, Kaunda RB, Zhou K (2018) Experimental investigations on the effects of ambient freeze-thaw cycling on dynamic properties and rock pore structure deterioration of sandstone. Cold Reg Sci Technol 154:133–141. https://doi.org/10.1016/j.coldregions.2018.06.015

Li S, Huo R, Yoshiaki F, Ren D, Song Z (2019) Effect of acid-temperature-pressure on the damage characteristics of sandstone. Int J Rock Mech Min Sci 122:104079. https://doi.org/10.1016/j.ijrmms.2019.104079

Li X, Shao Z, Qi C (2020) An analytical micro-macro model of stress drops during brittle creep in rocks. Eng Fract Mech 223:106794. https://doi.org/10.1016/j.engfracmech.2019.106794

Lin Y, Zhou K, Li J, Ke B, Gao R (2020) Weakening laws of mechanical properties of sandstone under the effect of chemical corrosion. Rock Mech Rock Eng 53(4):1857–1877. https://doi.org/10.1007/s00603-019-01998-z

Liu Y, Dai F (2018) A damage constitutive model for intermittent jointed rocks under cyclic uniaxial compression. Int J Rock Mech Min Sci 103:289–301. https://doi.org/10.1016/j.ijrmms.2018.01.046

Liu Z, Yang H, Wang W, Cheng W, Xin L (2018) Experimental study on the pore structure fractals and seepage characteristics of a coal sample around a borehole in coal seam water infusion. Transp Porous Media 125(2):289–309. https://doi.org/10.1007/s11242-018-1119-x

Liu H, Li L, Li S, Yang W (2020) The time-dependent failure mechanism of rocks and associated application in slope engineering: An explanation based on numerical investigation. Math Probl Eng 2020:1680265. https://doi.org/10.1155/2020/1680265

Lu Y, Wang L, Ge Z, Zhou Z, Deng K, Zuo S (2020) Fracture and pore structure dynamic evolution of coals during hydraulic fracturing. Fuel 259:116272. https://doi.org/10.1016/j.fuel.2019.116272

Lyu C, Ning Z, Cole DR, Wang Q, Chen M (2020) Experimental investigation on T2 cutoffs of tight sandstones: Comparisons between outcrop and reservoir cores. J Petrol Sci Eng 191:107184. https://doi.org/10.1016/j.petrol.2020.107184

Ma L, Liu X, Fang Q, Xu H, Xia H, Li E, Li W (2012) A new elasto-viscoplastic damage model combined with the generalized Hoek-Brown failure criterion for bedded rock salt and its application. Rock Mech Rock Eng 46(1):53–66. https://doi.org/10.1007/s00603-012-0256-8

Ma D, Duan H, Li X, Li Z, Zhou Z, Li T (2019) Effects of seepage-induced erosion on nonlinear hydraulic properties of broken red sandstones. Tunn Undergr Space Technol 91:102993. https://doi.org/10.1016/j.tust.2019.102993

Main IG (2000) A damage mechanics model for power-law creep and earthquake aftershock and foreshock sequences. Geophys J Int 142(1):11. https://doi.org/10.1046/j.1365-246x.2000.00136.x

Ngwenya BT, Main IG, Elphick SC, Crawford BR, Smart BGD (2001) A constitutive law for low-temperature creep of water-saturated sandstones. J Geophys Res 106(B10):21811–21826. https://doi.org/10.1029/2001JB000403

Nicksiar M, Martin CD (2013) Crack initiation stress in low porosity crystalline and sedimentary rocks. Eng Geol 154:64–76. https://doi.org/10.1016/j.enggeo.2012.12.007

Noël C, Pimienta L, Violay M (2019) Time-dependent deformations of sandstone during pore fluid pressure oscillations: Implications for natural and induced seismicity. J Geophys Res 124(1):801–821. https://doi.org/10.1029/2018JB016546

Paterson MS, Wong TF (2005) Experimental rock deformation-the brittle field, 2nd edn. Springer, Berlin

Shen Y, Wang Y, Wei X, Jia H, Yan R (2020) Investigation on meso-debonding process of the sandstone-concrete interface induced by freeze-thaw cycles using NMR technology. Constr Build Mater 252:118962. https://doi.org/10.1016/j.conbuildmat.2020.118962

Tang SB, Yu CY, Heap MJ, Chen PZ, Ren YG (2018) The influence of water saturation on the short- and long-term mechanical behavior of red sandstone. Rock Mech Rock Eng 51(9):2669–2687. https://doi.org/10.1007/s00603-018-1492-3

Tian H, Chen W, Yang D, Gong Z (2015) Experimental and numerical analysis of the time-dependent behaviour of argillaceous red sandstone under high in situ stress. Bull Eng Geol Env 74(2):567–575

Tsai LS, Hsieh YM, Weng MC, Huang TH, Jeng FS (2008) Time-dependent deformation behaviors of weak sandstones. Int J Rock Mech Min Sci 45(2):144–154. https://doi.org/10.1016/j.ijrmms.2007.04.008

Wang M, Cai M (2020) A grain-based time-to-failure creep model for brittle rocks. Comput Geotech 119:103344. https://doi.org/10.1016/j.compgeo.2019.103344

Wang R, Li L, Simon R (2019) A model for describing and predicting the creep strain of rocks from the primary to the tertiary stage. Int J Rock Mech Min Sci 123:104087. https://doi.org/10.1016/j.ijrmms.2019.104087

Wang C, Liu J, Chen L, Liu J, Wang L (2020a) Mechanical behaviour and damage evolution of Beishan granite considering the transient and time-dependent effects of excavation unloading. Eur J Environ Civil Eng. https://doi.org/10.1080/19648189.2020.1784292

Wang F, Cao P, Wang Y, Hao R, Meng J, Shang J (2020b) Combined effects of cyclic load and temperature fluctuation on the mechanical behavior of porous sandstones. Eng Geol 266:105466. https://doi.org/10.1016/j.enggeo.2019.105466

Wen T, Tang H, Ma J, Wang Y (2018) Evaluation of methods for determining crack initiation stress under compression. Eng Geol 235:81–97. https://doi.org/10.1016/j.enggeo.2018.01.018

Weng L, Wu Z, Li X (2018) Mesodamage characteristics of rock with a pre-cut opening under combined static–dynamic loads: a nuclear magnetic resonance (NMR) investigation. Rock Mech Rock Eng 51(8):2339–2354. https://doi.org/10.1007/s00603-018-1483-4

Weng L, Wu Z, Liu Q (2019) Evaluating damage and microcracking behavior of granite using NMR testing under different levels of unconfined compression. Int J Geomech 19(1):04018186. https://doi.org/10.1061/(ASCE)GM.1943-5622.0001335

Weng L, Wu Z, Liu Q, Chu Z, Zhang S (2021) Evolutions of the unfrozen water content of saturated sandstones during freezing process and the freeze-induced damage characteristics. Int J Rock Mech Min Sci 142:104757. https://doi.org/10.1016/j.ijrmms.2021.104757

Wong T-F, Baud P (2012) The brittle-ductile transition in porous rock: a review. J Struct Geol 44:25–53. https://doi.org/10.1016/j.jsg.2012.07.010

Wu XY, Baud P, Wong T (2000) Micromechanics of compressive failure and spatial evolution of anisotropic damage in Darley Dale sandstone. Int J Rock Mech Min Sci 37(1):143–160. https://doi.org/10.1016/S1365-1609(99)00093-3

Wu K, Shao Z, Qin S (2020) An analytical design method for ductile support structures in squeezing tunnels. Archiv Civ Mech Eng 20(3):91. https://doi.org/10.1007/s43452-020-00096-0

Xue DJ, Zhou HW, Liu YT, Deng LS, Zhang L (2018) Study of drainage and percolation of nitrogen-water flooding in tight coal by NMR imaging. Rock Mech Rock Eng 51(11):3421–3437. https://doi.org/10.1007/s00603-018-1473-6

Yang SQ, Hu B (2018) Creep and long-term permeability of a red sandstone subjected to cyclic loading after thermal treatments. Rock Mech Rock Eng 51(10):2981–3004. https://doi.org/10.1007/s00603-018-1528-8

Yang SQ, Jiang Y (2010) Triaxial mechanical creep behavior of sandstone. Mining Sci Technol 20(3):339–349. https://doi.org/10.1016/s1674-5264(09)60206-4

Yang SQ, Jing HW, Cheng L (2014a) Influences of pore pressure on short-term and creep mechanical behavior of red sandstone. Eng Geol 179(10):10–23. https://doi.org/10.1016/j.enggeo.2014.06.016

Yang W, Zhang Q, Li S, Wang S (2014b) Time-dependent behavior of diabase and a nonlinear creep model. Rock Mech Rock Eng 47(4):1211–1224. https://doi.org/10.1007/s00603-013-0478-4

Yang S, Hu B, Ranjith P, Xu P (2018) Multi-step loading creep behavior of red sandstone after thermal treatments and a creep damage model. Energies 11(1):10. https://doi.org/10.3390/en11010212

Yu C, Tang S, Tang CA, Duan D, Zhang Y, Ma T (2019) The effect of water on the creep behavior of red sandstone. Eng Geol 253:64–74. https://doi.org/10.1016/j.enggeo.2019.03.016

Yu J, Yao W, Duan K, Liu X, Zhu Y (2020) Experimental study and discrete element method modeling of compression and permeability behaviors of weakly anisotropic sandstones. Int J Rock Mech Min Sci 134:104437. https://doi.org/10.1016/j.ijrmms.2020.104437

Zhang Y, Shao J, Xu W, Jia Y, Zhao H (2015) Creep behaviour and permeability evolution of cataclastic sandstone in triaxial rheological tests. Eur J Environ Civ Eng 19(4):496–519. https://doi.org/10.1080/19648189.2014.960103

Zhao Y, Zhang L, Wang W, Wan W, Ma W (2018) Separation of elastoviscoplastic strains of rock and a nonlinear creep model. Int J Geomech 18(1):04017129. https://doi.org/10.1061/(ASCE)GM.1943-5622.0001033

Zheng H, Feng X, Hao X (2015) A creep model for weakly consolidated porous sandstone including volumetric creep. Int J Rock Mech Min Sci 78:99–107. https://doi.org/10.1016/j.ijrmms.2015.04.021

Zheng Z, Sun W, Fish J (2016) Micropolar effect on the cataclastic flow and brittle-ductile transition in high-porosity rocks. J Geophys Res 121(3):1425–1440. https://doi.org/10.1002/2015JB012179

Zhou K, Liu T, Hu Z (2018a) Exploration of damage evolution in marble due to lateral unloading using nuclear magnetic resonance. Eng Geol 244:75–85. https://doi.org/10.1016/j.enggeo.2018.08.001

Zhou X, Huang X, Berto F (2018b) A three-dimensional long-term strength criterion of rocks based on micromechanical method. Theoret Appl Fract Mech 97:409–418. https://doi.org/10.1016/j.tafmec.2017.07.003

Zhu W, Li S, Li S, Niu L (2019) Influence of dynamic disturbance on the creep of sandstone: An experimental study. Rock Mech Rock Eng 52(4):1023–1039. https://doi.org/10.1007/s00603-018-1642-7